We are IntechOpen, the world's leading publisher of Open Access books Built by scientists, for scientists

4,800
Open access books available

122,000
International authors and editors

135M
Downloads

Our authors are among the

154
Countries delivered to

TOP 1%
most cited scientists

12.2%
Contributors from top 500 universities

WEB OF SCIENCE™

Selection of our books indexed in the Book Citation Index in Web of Science™ Core Collection (BKCI)

Interested in publishing with us?
Contact book.department@intechopen.com

Numbers displayed above are based on latest data collected.
For more information visit www.intechopen.com

6

Review of the Magnetohydrodynamic Waves and Their Stability in Solar Spicules and X-Ray Jets

Ivan Zhelyazkov
Faculty of Physics, Sofia University
Bulgaria

1. Introduction

One of the most enduring mysteries in solar physics is why the Sun's outer atmosphere, or corona, is millions of kelvins hotter than its surface. Among suggested theories for coronal heating is one that considers the role of spicules – narrow jets of plasma shooting up from just above the Sun's surface – in that process (Athay & Holzer, 1982; Athay, 2000). For decades, it was thought that spicules might be sending heat into the corona. However, following observational research in the 1980s, it was found that spicule plasma did not reach coronal temperatures, and so this line of study largely fell out of vogue. Kukhianidze et al. (Kukhianidze et al., 2006) were first to report the observation of kink waves in solar spicules – the wavelength was found to be $\sim$3500 km, and the period of waves has been estimated to be in the range of 35–70 s. The authors argue that these waves may carry photospheric energy into the corona and therefore can be of importance in coronal heating. Zaqarashvili et al. (Zaqarashvili et al., 2007) analyzed consecutive height series of Hα spectra in solar limb spicules at the heights of 3800–8700 km above the photosphere and detected Doppler-shift oscillations with periods of 20–25 and 75–110 s. According to authors, the oscillations can be caused by waves' propagation in thin magnetic flux tubes anchored in the photosphere. Moreover, observed waves can be used as a tool for spicule seismology, and the magnetic filed induction in spicules at the height of $\sim$6000 km above the photosphere is estimated as 12–15 G. De Pontieu et al. (De Pontieu et al., 2007) identified a new class of spicules (see Fig. 1) that moved much faster and were shorter lived than the traditional spicules, which have speeds of between 20 and 40 km s^{-1} and lifespans of 3 to 7 minutes. These Type II spicules, observed in Ca II 854.2 nm and Hα lines (Sterling et al., 2010), are much more dynamic: they form rapidly (in $\sim$10 s), are very thin ($\leqslant$200 km wide), have lifetimes of 10 to 150 s (at any one height), and shoot upwards at high speeds, often in excess of 100–150 km s^{-1}, before disappearing. The rapid disappearance of these jets had suggested that the plasma they carried might get very hot, but direct observational evidence of this process was missing. Both types of spicules are observed to carry Alfvén waves with significant amplitudes of order 20 km s^{-1}. In a recent paper, De Pontieu et al. (De Pontieu et al., 2011) used new observations from the Atmospheric Imaging Assembly on NASA's recently launched *Solar Dynamics Observatory* and its Focal Plane Package for the Solar Optical Telescope (SOT) on the Japanese *Hinode* satellite. Their observations reveal "a ubiquitous coronal mass supply in which chromospheric plasma in fountainlike jets or spicules (see Fig. 2) is accelerated upward into the corona, with much of the plasma heated to temperatures between $\sim$0.02 and 0.1 million kelvin (MK) and a small but sufficient fraction to temperatures above 1 MK. These observations provide constraints

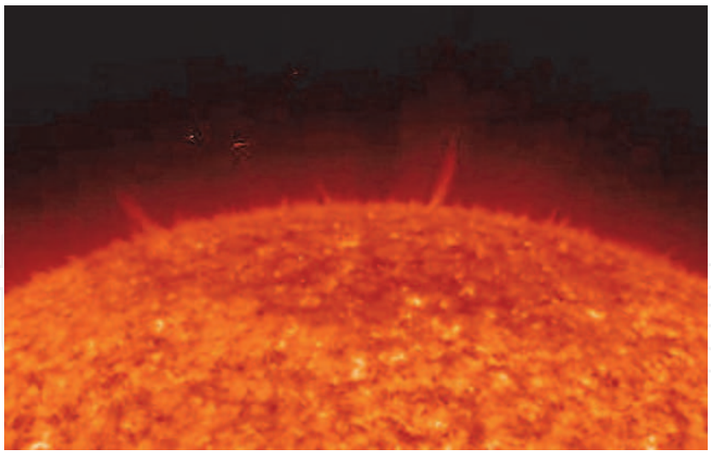

Fig. 1. Solar spicules on the Sun recorded on August 3, 2007. Credit: NASA/*STEREO*.

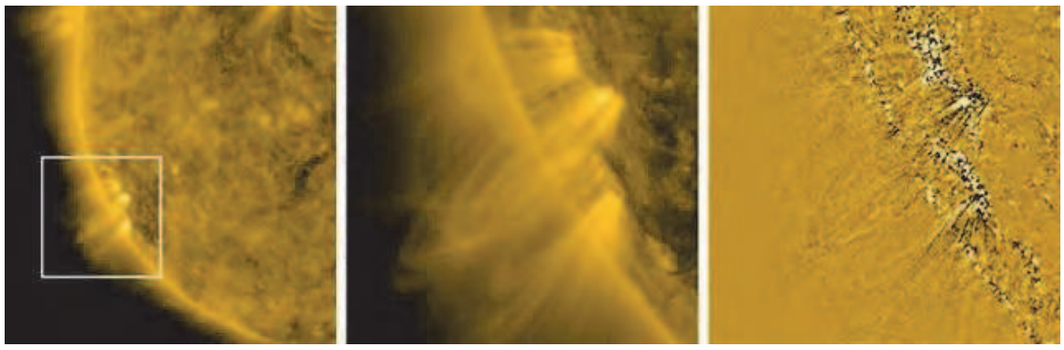

Fig. 2. Solar spicules recorded by the *Solar Dynamics Observatory* on April 25, 2010. Credit: NASA/*SDO*.

on the coronal heating mechanism(s) and highlight the importance of the interface region between photosphere and corona." Nevertheless, Moore et al. (Moore et al., 2011) from *Hinode* observations of solar X-ray jets, Type II spicules, and granule-size emerging bipolar magnetic fields in quiet regions and coronal holes, advocate a scenario for powering coronal heating and the solar wind. In this scenario, Type II spicules and Alfvén waves are generated by the granule-size emerging bipoles in the manner of the generation of X-ray jets by larger magnetic bipoles. From observations and this scenario, the authors estimate that Type II spicules and their co-generated Alfvén waves carry into the corona an area-average flux of mechanical energy of $\sim 7 \times 10^5$ erg s^{-1} cm^{-2}. This is enough to power the corona and solar wind in quiet regions and coronal holes, hence indicates that the granule-size emerging bipoles are the main engines that generate and sustain the entire heliosphere. The upward propagation of high- and low-frequency Alfvén waves along spicules detected from SOT's observations on *Hinode* was also reported by He et al. (He et al, 1999) and Tavabi et al. (Tavabi et al., 2011). He et al. found in four cases that the spicules are modulated by high-frequency ($\geqslant$0.02 Hz) transverse fluctuations. These fluctuations are suggested to be Alfvén waves that propagate upwards along the spicules with phase speed ranges from 50 to 150 km s^{-1}. Three of the modulated spicules show clear wave-like shapes with short wavelengths less than 8 Mm. We note that at the same time, Kudoh & Shibata (Kudoh & Shibata, 1999) presented a torsional Alfvén-wave model of spicules (actually the classical Type I spicules) and discussed the possibility for wave

coronal heating – the energy flux transported into corona was estimated to be of about 3×10^5 erg s^{-1} cm^{-2}, i.e., roughly half of the flux carried by the Alfvén waves running on Type II spicules (Moore et al., 2011). Tavabi et al. (Tavabi et al., 2011), performed a statistical analysis of the SOT/*Hinode* observations of solar spicules and their wave-like behavior, and argued that there is a possible upward propagation of Alfvén waves inside a doublet spicule with a typical wave's period of 110 s.

No less effective in coronal heating are the so called X-ray jets. We recall, however, that whilst the classical spicules were first discovered in 1870's by the Jesuit astronomer Pietro Angelo Secchi (Secchi, 1877) and named as "spicules" by Roberts (Roberts, 1945), the X-ray jets are relatively a new discovered phenomenon. They, the jets, were extensively observed with the Soft X-ray Telescope on *Yohkoh* (Shibata et al., 1992; Shimojo et al., 1996), and their structure and dynamics have been better resolved by the X-Ray Telescope (XRT) on *Hinode*, in movies having 1 arc sec pixels and ∼1-minute cadence (Cirtain et al., 2007) – see Fig. 3. According

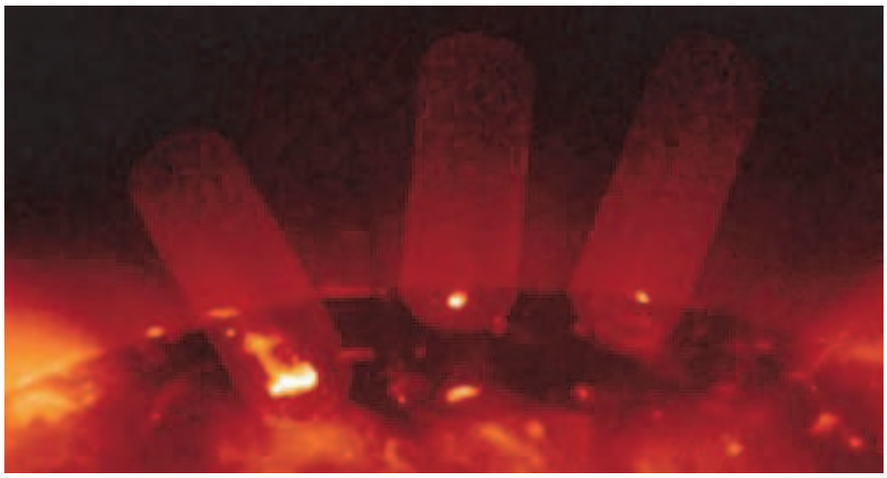

Fig. 3. Three X-ray jets recorded by the *Hinode* spacecraft on January 10, 2007. Credit: SAO/NASA/JAXA/NAOJ.

to Cirtain et al. (Cirtain et al., 2007), "coronal magnetic fields are dynamic, and field lines may misalign, reassemble, and release energy by means of magnetic reconnection. Giant releases may generate solar flares and coronal mass ejections and, on a smaller scale, produce X-ray jets. *Hinode* observations of polar coronal holes reveal that X-ray jets have two distinct velocities: one near the Alfvén speed (∼800 kilometers per second) and another near the sound speed (200 kilometers per second). The X-ray jets are from 2×10^3 to 2×10^4 kilometers wide and 1×10^5 kilometers long and last from 100 to 2500 seconds. The large number of events, coupled with the high velocities of the apparent outflows, indicates that the jets may contribute to the high-speed solar wind." The more recent observations (Madjarska, 2011; Shimojo & Shibata, 2000) yield that the temperature of X-ray jets is from 1.3 to 12 MK (i.e., the jets are hotter than the ambient corona) and the electron/ion number density is of about $(0.7–4) \times 10^9$ cm^{-3} with average of 1.7×10^9 cm^{-3}. The X-ray jets can have velocities above 10^3 km s^{-1}, reach heights of a solar radius or more, and have kinetic energies of the order of 10^{29} erg.

Since both spicules and X-ray jets support Alfvén (or more generally magnetohydrodynamic) waves' propagation it is of great importance to determine their dispersion characteristics

and more specifically their stability/instability status. If while propagating along the jets MHD waves become unstable and the expected instability is of the Kelvin–Helmholtz type, that instability can trigger the onset of wave turbulence leading to an effective plasma jet heating and the acceleration of the charged particles. We note that the Alfvénic turbulence is considered to be the most promising source of heating in the chromosphere and extended corona (van Ballegooijen et al., 2011). In this study, we investigate these travelling wave properties for a realistic, cylindrical geometry of the spicules and X-ray jets considering appropriate values for the basic plasma jet parameters (mass density, magnetic fields, sound, Alfvén, and jet speeds), as well as those of the surrounding medium. For detailed reviews of the oscillations and waves in magnetically structured solar spicules we refer the reader to (Zaqarashvili & Erdélyi, 2009) and (Zaqarashvili, 2011). Our research concerns the dispersion curves of kink and sausage modes for the MHD waves travelling primarily along the Type II spicules and X-ray jets for various values of the jet speed. In studying wave propagation characteristics, we assume that the axial wave number k_z ($\hat{z}$ is the direction of the embedded constant magnetic fields in the two media) is real, while the angular wave frequency, ω, is complex. The imaginary part of that complex frequency is the wave growth rate when a given mode becomes unstable. All of our analysis is based on a linearized set of equations for the adopted form of magnetohydrodynamics. We show that the stability/instability status of the travelling waves depends entirely on the magnitudes of the flow velocities and the values of two important control parameters, namely the so-called density contrast (the ratio of the mass density inside to that outside the flux tube) and the ratio of the background magnetic field of the environment to that of the spicules and X-ray jets.

2. Geometry and basic magnetohydrodynamic equations

The simplest model of spicules is a straight vertical cylinder (see Fig. 4) with radius a

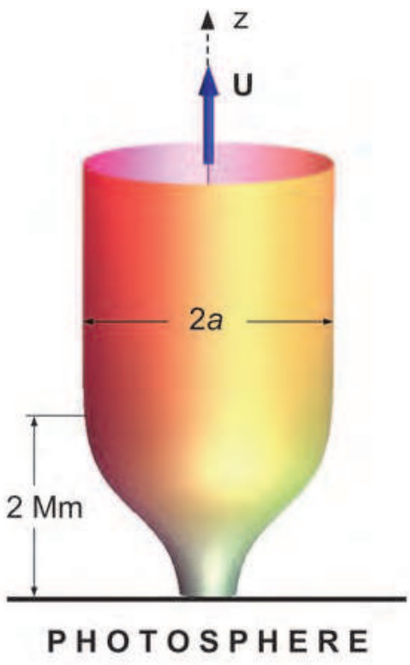

Fig. 4. Geometry of a spicule flux tube containing flowing plasma with velocity **U**.

filled with ideal compressible plasma of density $\rho_{\rm i} \sim 3 \times 10^{-13}$ g cm^{-3} (Sterling, 2000) and immersed in a constant magnetic field $\mathbf{B}_{\rm i}$ directed along the z axis. Such a cylinder is usually termed *magnetic flux tube* or simply 'flux tube.' The most natural discontinuity, which occurs at the surface binding the cylinder, is the tangential one because it is the discontinuity that ensures an equilibrium total pressure balance. Moreover, it is worth noting that the jet is non-rotating and without twist – otherwise the centrifugal and the magnetic tension forces should be taken into account. Due to the specific form of the real flux tube which models a spicule, that part of the whole flux tube having a constant radius actually starts at the height of 2 Mm from the tube footpoint. The flow velocity, $\mathbf{U}_{\rm i}$, like the ambient magnetic field, is directed along the z axis. The mass density of the environment, $\rho_{\rm e}$, is much, say 50–100 times, less than that of the spicule, while the magnetic field induction $B_{\rm e}$ might be of the order or less than $B_{\rm i} \sim$ 10–15 G. Both the magnetic field, $\mathbf{B}_{\rm e}$, and flow velocity, $\mathbf{U}_{\rm e}$ (if any), are also in the $\hat{z}$-direction. We note that while the parameters of classical Type I spicules are well-documented (Beckers, 1968; 1972) those of Type II spicules are generally disputed; Centeno et al. (Centeno et al., 2010), for example, on using a novel inversion code for Stokes profiles caused by the joint action of atomic level polarization and the Hanle and Zeeman effects to interpret the observations, claim that magnetic fields as strong as ∼50 G were detected in a very localized area of the slit, which might represent a lower field strength of organized network spicules.

The flux tube modelling of the X-ray jets is actually the same as that for spicules, however, with different magnitudes of the mass densities, flow velocities, and background magnetic fields. When studying waves' propagation and their stability/instability status for a given solar structure (spicule or X-ray jet), the values of the basic parameters will be additionally specified. Now let us see what are the basic magnetohydrodynamic equations governing the motions in a flowing solar plasma.

2.1 Basic equations of ideal magnetohydrodynamics

Magnetohydrodynamics (MHD) studies the dynamics of electrically conducting fluids. Examples of such fluids include plasmas and liquid metals. The field of MHD was initiated in 1942 by the Swedish physicist Hannes Alfvén (1908–1995), who received the Nobel Prize in Physics (1970) for "fundamental work and discoveries in magnetohydrodynamics with fruitful applications in different parts of plasma physics." The fundamental concept behind MHD is that magnetic fields can induce currents in a moving conductive fluid, which in turn creates forces on the fluid and also changes the magnetic field itself. The set of equations, which describe MHD are a combination of the equations of motion of fluid dynamics (Navier–Stokes equations) and Maxwell's equations of electromagnetism. These partial differential equations have to be solved simultaneously, either analytically or numerically.

Magnetohydrodynamics is a macroscopic theory. Its equations can in principle be derived from the kinetic Boltzmann's equation assuming space and time scales to be larger than all inherent scale-lengths such as the Debye length or the gyro-radii of the charged particles (Chen, 1995). It is, however, more convenient to obtain the MHD equations in a phenomenological way as an electromagnetic extension of the hydrodynamic equations of ordinary fluids, where the main approximation is to neglect the displacement current $\propto \partial \mathbf{E}/\partial t$ in Ampère's law.

In the standard nonrelativistic form the MHD equations consist of the basic conservation laws of mass, momentum, and energy together with the induction equation for the magnetic field. Thus, the MHD equations of our magnetized quasineutral plasma with singly charged ions (and electrons) are

$$\frac{\partial \rho}{\partial t} + \nabla \cdot \rho \mathbf{v} = 0, \tag{1}$$

where ρ is the mass density and $\mathbf{v}$ is the bulk fluid velocity. Equation (1) is the so called *continuity equation* in our basis set of equations.

The momentum equation is

$$\frac{\partial (\rho \mathbf{v})}{\partial t} + \rho(\mathbf{v} \cdot \nabla)\mathbf{v} = \mathbf{j} \times \mathbf{B} - \nabla p + \rho \mathbf{g}, \tag{2}$$

where $\mathbf{j} \times \mathbf{B}$ (with $\mathbf{j}$ being the current density and $\mathbf{B}$ magnetic field induction) is the *Lorentz force* term, $-\nabla p$ is the pressure-gradient term, and $\rho \mathbf{g}$ is the gravity force.

Faraday's law reads

$$\frac{\partial \mathbf{B}}{\partial t} = -\nabla \times \mathbf{E}, \tag{3}$$

where $\mathbf{E}$ is the electric field. The ideal Ohm's law for a plasma, which yields a useful relation between electric and magnetic fields, is

$$\mathbf{E} + \mathbf{v} \times \mathbf{B} = 0. \tag{4}$$

The low-frequency Ampère's law, which neglects the displacement current, is given by

$$\mu_0 \mathbf{j} = \nabla \times \mathbf{B}, \tag{5}$$

where μ_0 is the permeability of free space.

The magnetic divergency constraint is

$$\nabla \cdot \mathbf{B} = 0. \tag{6}$$

By determining the current density $\mathbf{j}$ from Ampère's Eq. (5), the expression of the Lorentz force can be presented in the form

$$\mathbf{j} \times \mathbf{B} = \frac{1}{\mu_0}(\mathbf{B} \cdot \nabla)\mathbf{B} - \nabla \left(\frac{B^2}{2\mu_0} \right),$$

where the first term on the right hand side is the magnetic tension force and the second term is the magnetic pressure force. Thus, momentum Eq. (2) can be rewritten in a more convenient form, notably

$$\frac{\partial (\rho \mathbf{v})}{\partial t} + \rho(\mathbf{v} \cdot \nabla)\mathbf{v} = -\nabla \left(p + \frac{B^2}{2\mu_0} \right) + \frac{1}{\mu_0}(\mathbf{B} \cdot \nabla)\mathbf{B} + \rho \mathbf{g}. \tag{7}$$

On the other hand, on using Ohm's law (4) the Faraday's law (or induction equation) takes the form

$$\frac{\partial \mathbf{B}}{\partial t} = -\nabla \times (\mathbf{v} \times \mathbf{B}). \tag{8}$$

Finally, the equation of the thermal energy is given by

$$\frac{\mathrm{d}}{\mathrm{d}t}\frac{p}{\rho^{\gamma}} = 0,$$

where $\gamma = 5/3$ is the ratio of specific heats for an adiabatic equation of state. This equation usually is written as an equation for the pressure, p,

$$\frac{\partial p}{\partial t} + \mathbf{v}\cdot\nabla p + \gamma p \nabla\cdot\mathbf{v} = 0. \tag{9}$$

Equation (9) implies that the equation of state of the ideal fully ionized gas has the form

$$p = 2(\rho/m_{\mathrm{i}})k_{\mathrm{B}}T,$$

where T is the temperature, m_{i} the ion mass, k_{B} is the Boltzmann constant, and the factor 2 arises because ions and electrons contribute equally.

In total the ideal MHD equations thus consist of two vector equations, (7) and (8), and two scalar equations, (1) and (9), respectively. Occasionally, when studying wave propagation in magnetized plasmas, one might also be necessary to use Eq. (6). We note that the basic variables of the ideal MHD are the mass density, ρ, the fluid bulk velocity, $\mathbf{v}$, the pressure, p, and the magnetic induction, $\mathbf{B}$; the electric field, $\mathbf{E}$, has been excluded via Ohm's law.

In MHD there is a few dimensionless numbers, which are widely used in studying various phenomena in magnetized plasmas. Such an important dimensionless number in MHD theory is the plasma beta, β, defined as the ratio of gas pressure, p, to the magnetic pressure,

$$\beta = \frac{p}{B^2/2\mu_0}.$$

When the magnetic field dominates in the fluid, $\beta \ll 1$, the fluid is forced to move along with the field. In the opposite case, when the field is weak, $\beta \gg 1$, the field is swirled along by the fluid.

We finish our short introduction to MHD recalling that in ideal MHD Lenz's law dictates that the fluid is in a sense tied to the magnetic field lines, or, equivalently, magnetic filed lines are *frozen into the fluid*. To explain, in ideal MHD a small rope-like volume of fluid surrounding a field line will continue to lie along a magnetic field line, even as it is twisted and distorted by fluid flows in the system. The connection between magnetic field lines and fluid in ideal MHD fixes the topology of the magnetic field in the fluid.

3. Wave dispersion relations

It is well-known that in infinite magnetized plasmas there exist three types of MHD waves (Chen, 1995), namely the Alfvén wave and the fast and slow magnetoacoustic waves. Alfvén wave (Alfvén, 1942; Gekelman et al., 2011), is a transverse wave propagating at speed $v_{\mathrm{A}} = B_0/(\mu_0\rho_0)^{1/2}$, where B_0 and ρ_0 are the equilibrium (not perturbed) magnetic field and mass density, respectively. The propagation characteristics of magnetoacoustic waves depend upon their plasma beta environment. In particular, in high-beta plasmas ($\beta \gg 1$) the fast magnetoacoustic wave behaves like a sound wave travelling at sound speed $c_{\mathrm{s}} = (\gamma p_0/\rho_0)^{1/2}$, while in low-beta plasmas ($\beta \ll 1$) it propagates roughly isotropically and across

the magnetic field lines at Alfvén speed, $v_{\rm A}$. The slow magnetoacoustic wave in high-beta plasmas is guided along the magnetic field $\mathbf{B}_0$ at Alfvén speed, $v_{\rm A}$ – in the opposite case of low-beta plasmas it is a longitudinally propagating along $\mathbf{B}_0$ wave at sound speed, $c_{\rm s}$. A question that immediately raises is how these waves will change when the magnetized plasma is spatially bounded (or magnetically structured) as in our case of spicules or X-ray jets. The answer to that question is not trivial – we actually have to derive the *normal modes* supported by the flux tube, which models the jets.

As we will study a linear wave propagation, the basic MHD variables can be presented in the form

$$\rho = \rho_0 + \delta\rho, \quad p = p_0 + \delta p, \quad \mathbf{v} = \mathbf{U} + \delta\mathbf{v}, \quad \text{and} \quad \mathbf{B} = \mathbf{B}_0 + \delta\mathbf{B},$$

where ρ_0, p_0, and $\mathbf{B}_0$ are the equilibrium values in either medium, $\mathbf{U}_{\rm i}$ and $\mathbf{U}_{\rm e}$ are the flow velocities inside and outside the flux tube, $\delta\rho$, δp, $\delta\mathbf{v}$, and $\delta\mathbf{B}$ being the small perturbations of the basic MHD variables. For convenience, we chose the frame of reference to be attached to the ambient medium. In that case

$$\mathbf{U}^{\rm rel} = \mathbf{U}_{\rm i} - \mathbf{U}_{\rm e}$$

is the *relative* flow velocity whose magnitude is a non-zero number inside the jet, and zero in the surrounding medium. For spicules, $U_{\rm e} \approx 0$; which is why the relative flow velocity is indeed the jet velocity, which we later denote as simply $\mathbf{U}$.

With the above assumptions, the basic set of MHD equations for the perturbations of the mass density, pressure, fluid velocity, and magnetic field become

$$\frac{\partial}{\partial t}\delta\rho + (\mathbf{U}\cdot\nabla)\delta\rho + \rho_0\nabla\delta\mathbf{v} = 0, \tag{10}$$

$$\rho_0\frac{\partial}{\partial t}\delta\mathbf{v} + \rho_0\left(\mathbf{U}\cdot\nabla\right)\delta\mathbf{v} + \nabla\left(\delta p + \frac{1}{\mu_0}\mathbf{B}_0\cdot\delta\mathbf{B}\right) - \frac{1}{\mu_0}(\mathbf{B}_0\cdot\nabla)\delta\mathbf{B} = 0, \tag{11}$$

$$\frac{\partial}{\partial t}\delta\mathbf{B} + (\mathbf{U}\cdot\nabla)\delta\mathbf{B} - (\mathbf{B}_0\cdot\nabla)\delta\mathbf{v} + \mathbf{B}_0\nabla\cdot\delta\mathbf{v} = 0, \tag{12}$$

$$\frac{\partial}{\partial t}\delta p + (\mathbf{U}\cdot\nabla)\delta p + \gamma p_0\nabla\cdot\delta\mathbf{v} = 0, \tag{13}$$

$$\nabla\cdot\delta\mathbf{B} = 0. \tag{14}$$

We note that the gravity force term in momentum Eq. (11) has been omitted because one assumes that the mass density of the jet does not change appreciably in the limits of the spicule's length of order 10–11 Mm.

From Eq. (10) we obtain that

$$\nabla\cdot\delta\mathbf{v} = -\frac{1}{\rho_0}\left[\frac{\partial}{\partial t}\delta\rho + (\mathbf{U}\cdot\nabla)\delta\rho\right]. \tag{15}$$

Inserting this expression into Eq. (13) we get

$$\left[\frac{\partial}{\partial t} + (\mathbf{U}\cdot\nabla)\right]\delta p - c_{\rm s}^2\left[\frac{\partial}{\partial t} + (\mathbf{U}\cdot\nabla)\right]\delta\rho = 0,$$

which means that the pressure's and density's perturbations are related via the expression

$$\delta p = c_{\rm s}^2\delta\rho, \qquad \text{where} \qquad c_{\rm s} = \left(\gamma p_0/\rho_0\right)^{1/2}. \tag{16}$$

Assuming that each perturbation is presented as a plain wave $g(r)\exp\left[\mathrm{i}\left(-\omega t+m\varphi+k_z z\right)\right]$ with its amplitude $g(r)$ being just a function of r, and that in cylindrical coordinates the nabla operator has the form

$$\nabla \equiv \frac{\partial}{\partial r}\hat{r}+\frac{1}{r}\frac{\partial}{\partial \varphi}\hat{\varphi}+\frac{\partial}{\partial z}\hat{z},$$

Eq. (11) reads

$$-\mathrm{i}\rho_0(\omega-\mathbf{k}\cdot\mathbf{U})\delta v_r+\frac{\mathrm{d}}{\mathrm{d}r}\left(\delta p+\frac{1}{\mu_0}B_0\delta B_z\right)-\mathrm{i}k_z\frac{1}{\mu_0}B_0\delta B_r=0, \tag{17}$$

$$-\rho_0(\omega-\mathbf{k}\cdot\mathbf{U})\delta v_\varphi+\frac{m}{r}\left(\delta p+\frac{1}{\mu_0}B_0\delta B_z\right)-k_z\frac{1}{\mu_0}B_0\delta B_\varphi=0, \tag{18}$$

$$-\rho_0(\omega-\mathbf{k}\cdot\mathbf{U})\delta v_z+k_z\left(\delta p+\frac{1}{\mu_0}B_0\delta B_z\right)-k_z\frac{1}{\mu_0}B_0\delta B_z=0. \tag{19}$$

Accordingly Eq. (13) yields

$$-\mathrm{i}(\omega-\mathbf{k}\cdot\mathbf{U})\delta p+\gamma p_0\nabla\cdot\delta\mathbf{v}=0. \tag{20}$$

Induction Eq. (12) gives

$$(\omega-\mathbf{k}\cdot\mathbf{U})\delta B_r-k_z B_0\delta v_r=0, \tag{21}$$

$$(\omega-\mathbf{k}\cdot\mathbf{U})\delta B_\varphi-k_z B_0\delta v_\varphi=0, \tag{22}$$

$$-\mathrm{i}(\omega-\mathbf{k}\cdot\mathbf{U})\delta B_z-\mathrm{i}k_z B_0\delta v_z+B_0\nabla\cdot\delta\mathbf{v}=0. \tag{23}$$

Finally Eq. (14) yields

$$\frac{\mathrm{d}}{\mathrm{d}r}\delta B_r+\frac{1}{r}\delta B_r+\mathrm{i}\frac{m}{r}\delta B_\varphi+\mathrm{i}k_z\delta B_z=0. \tag{24}$$

From Eq. (19) we obtain

$$\delta v_z=\frac{k_z}{\omega-\mathbf{k}\cdot\mathbf{U}}\frac{1}{\rho_0}\delta p\quad\text{or}\quad\delta p=\rho_0\frac{\omega-\mathbf{k}\cdot\mathbf{U}}{k_z}\delta v_z, \tag{25}$$

while Eq. (20) gives

$$\delta p=-\mathrm{i}\frac{1}{\omega-\mathbf{k}\cdot\mathbf{U}}\gamma p_0\nabla\cdot\delta\mathbf{v},$$

which means that

$$\delta v_z=-\mathrm{i}\frac{k_z}{(\omega-\mathbf{k}\cdot\mathbf{U})^2}\frac{\gamma p_0}{\rho_0}\left(\frac{\mathrm{d}}{\mathrm{d}r}\delta v_r+\frac{1}{r}\delta v_r+\mathrm{i}\frac{m}{r}\delta v_\varphi+\mathrm{i}k_z\delta v_z\right).$$

After some rearranging this expression can be rewritten in the form

$$\frac{\mathrm{d}}{\mathrm{d}r}\delta v_r+\frac{1}{r}\delta v_r+\mathrm{i}\frac{m}{r}\delta v_\varphi=\mathrm{i}\frac{(\omega-\mathbf{k}\cdot\mathbf{U})^2-k_z^2c_\mathrm{s}^2}{k_z c_\mathrm{s}^2}\delta v_z \tag{26}$$

Let us now differentiate Eq. (17) with respect to r:

$$-\mathrm{i}\rho_0(\omega-\mathbf{k}\cdot\mathbf{U})\frac{\mathrm{d}}{\mathrm{d}r}\delta v_r+\frac{\mathrm{d}^2}{\mathrm{d}r^2}\left(\delta p+\frac{1}{\mu_0}B_0\delta B_z\right)-\frac{1}{\mu_0}B_0\mathrm{i}k_z\frac{\mathrm{d}}{\mathrm{d}r}\delta B_r=0. \tag{27}$$

But according to Eqs. (26) and (24)

$$\frac{\mathrm{d}}{\mathrm{d}r}\delta v_r = -\frac{1}{r}\delta v_r - \mathrm{i}\frac{m}{r}\delta v_\varphi - \mathrm{i}k_z\left[1 - \frac{(\omega - \mathbf{k}\cdot\mathbf{U})^2}{k_z^2 c_\mathrm{s}^2}\right]\delta v_z,$$

$$\frac{\mathrm{d}}{\mathrm{d}r}\delta B_r = -\frac{1}{r}\delta B_r - \mathrm{i}\frac{m}{r}\delta B_\varphi - \mathrm{i}k_z\delta B_z.$$

Then Eq. (27) becomes

$$\mathrm{i}\rho_0(\omega - \mathbf{k}\cdot\mathbf{U})\frac{1}{r}\delta v_r - \rho_0(\omega - \mathbf{k}\cdot\mathbf{U})\frac{m}{r}\delta v_\varphi - \rho_0(\omega - \mathbf{k}\cdot\mathbf{U})\left[1 - \frac{(\omega - \mathbf{k}\cdot\mathbf{U})^2}{k_z^2 c_\mathrm{s}^2}\right]k_z\delta v_z$$
$$+ \frac{\mathrm{d}^2}{\mathrm{d}r^2}\left(\delta p + \frac{1}{\mu_0}B_0\delta B_z\right) + \frac{1}{\mu_0}B_0\mathrm{i}k_z\frac{1}{r}\delta B_r - \frac{1}{\mu_0}B_0 k_z\frac{m}{r}\delta B_\varphi - \frac{1}{\mu_0}B_0 k_z^2\delta B_z = 0 \quad (28)$$

In order to simplify notation we introduce a new variable, namely the perturbation of the total pressure, $\delta p_\mathrm{tot} = \delta p + \frac{1}{\mu_0}B_0\delta B_z$. From Eqs. (17) to (19) one can get that

$$\frac{1}{\mu_0}B_0\mathrm{i}k_z\frac{1}{r}\delta B_r = -\mathrm{i}\rho_0(\omega - \mathbf{k}\cdot\mathbf{U})\frac{1}{r}\delta v_r + \frac{1}{r}\frac{\mathrm{d}}{\mathrm{d}r}\delta p_\mathrm{tot},$$

$$-\frac{1}{\mu_0}B_0\mathrm{i}k_z\frac{m}{r}\delta B_\varphi = \rho_0(\omega - \mathbf{k}\cdot\mathbf{U})\frac{m}{r}\delta v_\varphi - \frac{m^2}{r^2}\delta p_\mathrm{tot},$$

$$-\frac{1}{\mu_0}B_0\mathrm{i}k_z^2\delta B_z = \rho_0(\omega - \mathbf{k}\cdot\mathbf{U})k_z\delta v_z - k_z^2\delta p_\mathrm{tot}.$$

Inserting these expressions into Eq. (28), we obtain

$$\left[\frac{\mathrm{d}^2}{\mathrm{d}r^2} + \frac{1}{r}\frac{\mathrm{d}}{\mathrm{d}r} - \left(k_z^2 + \frac{m^2}{r^2}\right)\right]\delta p_\mathrm{tot} + \rho_0\frac{(\omega - \mathbf{k}\cdot\mathbf{U})^3}{k_z c_\mathrm{s}^2}\delta v_z = 0. \quad (29)$$

Bearing in mind that according to Eq. (15)

$$\nabla\cdot\delta\mathbf{v} = \mathrm{i}(\omega - \mathbf{k}\cdot\mathbf{U})\frac{\delta\rho}{\rho_0},$$

from Eq. (23) we get

$$(\omega - \mathbf{k}\cdot\mathbf{U})\delta B_z - k_z B_0\delta v_z + B_0(\omega - \mathbf{k}\cdot\mathbf{U})\frac{\delta\rho}{\rho_0} = 0.$$

On using Eq. (16) we express $\delta\rho$ in the above equation as $\delta p/c_\mathrm{s}^2$, multiply it by

$$-\frac{1}{\mu_0}B_0\frac{1}{\omega - \mathbf{k}\cdot\mathbf{U}}$$

to get after some algebra that

$$\delta p + \frac{1}{\mu_0}B_0\delta B_z = -\frac{k_z\rho_0}{\omega - \mathbf{k}\cdot\mathbf{U}}\frac{B_0^2}{\mu_0\rho_0}\delta v_z + \delta p\left(1 + \frac{v_\mathrm{A}^2}{c_\mathrm{s}^2}\right),$$

where, we remember, $v_{\mathrm{A}} = B_0/(\mu_0\rho_0)^{1/2}$ is the Alfvén speed. After inserting in the above equation δp expressed in terms of δv_z – see Eq. (25) – and performing some straightforward algebra we obtain that

$$\delta v_z = -\frac{1}{\rho_0}\frac{\omega - \mathbf{k}\cdot\mathbf{U}}{k_z}\frac{k_z^2 c_{\mathrm{s}}^2}{k_z^2 c_{\mathrm{s}}^2 v_{\mathrm{A}}^2 - (\omega - \mathbf{k}\cdot\mathbf{U})^2\left(c_{\mathrm{s}}^2 + v_{\mathrm{A}}^2\right)}\delta p_{\mathrm{tot}}.$$

Next step is to insert above expression of δv_z into Eq. (29) and combine the $-k_z^2\,\delta p$-term with the last member in the same equation to get a new form of Eq. (29), notably

$$\left[\frac{\mathrm{d}^2}{\mathrm{d}r^2} + \frac{1}{r}\frac{\mathrm{d}}{\mathrm{d}r} - \left(\kappa^2 + \frac{m^2}{r^2}\right)\right]\delta p_{\mathrm{tot}} = 0. \tag{30}$$

Here, κ^2 is given by the expression

$$\kappa^2 = -\frac{\left[(\omega - \mathbf{k}\cdot\mathbf{U})^2 - k_z^2 c_{\mathrm{s}}^2\right]\left[(\omega - \mathbf{k}\cdot\mathbf{U})^2 - k_z^2 v_{\mathrm{A}}^2\right]}{\left(c_{\mathrm{s}}^2 + v_{\mathrm{A}}^2\right)\left[(\omega - \mathbf{k}\cdot\mathbf{U})^2 - k_z^2 c_{\mathrm{T}}^2\right]}, \tag{31}$$

where

$$c_{\mathrm{T}} = \frac{c_{\mathrm{s}} v_{\mathrm{A}}}{\left(c_{\mathrm{s}}^2 + v_{\mathrm{A}}^2\right)^{1/2}} \tag{32}$$

is the so-called *tube velocity* (Edwin & Roberts, 1983). It is important to notice that both κ^2 (respectively κ) and the tube velocity, c_{T}, *have different values inside and outside the jet* due to the different sound and Alfvén speeds, which characterize correspondingly the jet and its surrounding medium.

As can be seen, Eq. (30) is the equation for the modified Bessel functions I_m and K_m and, accordingly, its solutions in both media (the jet and its environment) are:

$$\delta p_{\mathrm{tot}}(r) = \begin{cases} A_{\mathrm{i}} I_m(\kappa_{\mathrm{i}} r) & \text{for } r \leqslant a, \\ A_{\mathrm{e}} K_m(\kappa_{\mathrm{e}} r) & \text{for } r \geqslant a. \end{cases}$$

From Eq. (17) one can obtain an expression of δv_r and inserting it in the expression of δB_r deduced from Eq. (21) one gets a formula relating δv_r with the first derivative (with respect to r) of δp_{tot}

$$\delta v_r = -\frac{\mathrm{i}}{\rho_0}\frac{\omega - \mathbf{k}\cdot\mathbf{U}}{(\omega - \mathbf{k}\cdot\mathbf{U})^2 - k_z^2 v_{\mathrm{A}}^2}\frac{\mathrm{d}}{\mathrm{d}r}\delta p_{\mathrm{tot}}. \tag{33}$$

It is clear that we have two different expressions of δv_r, which, bearing in mind the solutions to the ordinary second order differential Eq. (30), read

$$\delta v_r(r \leqslant a) = -\frac{\mathrm{i}}{\rho_{\mathrm{i}}}\frac{\omega - \mathbf{k}\cdot\mathbf{U}}{(\omega - \mathbf{k}\cdot\mathbf{U})^2 - k_z^2 v_{\mathrm{Ai}}^2}\kappa_{\mathrm{i}} A_{\mathrm{i}} I_m'(\kappa_{\mathrm{i}} r)$$

and

$$\delta v_r(r \geqslant a) = -\frac{\mathrm{i}}{\rho_{\mathrm{e}}}\frac{\omega}{\omega^2 - k_z^2 v_{\mathrm{Ae}}^2}\kappa_{\mathrm{e}} A_{\mathrm{e}} K_m'(\kappa_{\mathrm{e}} r),$$

respectively. Now it is time to apply some boundary conditions, which link the solutions of total pressure and fluid velocity perturbations at the interface $r = a$. The appropriate boundary conditions are:

- δp_{tot} has to be continuous across the interface,
- the perturbed interface, $\dfrac{\delta v_r}{\omega - \mathbf{k}\cdot\mathbf{U}}$, has also to be continuous (Chandrasekhar, 1961).

After applying the boundary conditions (we recall that for the ambient medium $U = 0$) finally we arrive at the required dispersion relation of the normal MHD modes propagating along the jet (Nakariakov, 2007; Terra-Homen et al., 2003)

$$\frac{\rho_{\mathrm{e}}}{\rho_{\mathrm{i}}}\left(\omega^2 - k_z^2 v_{\mathrm{Ae}}^2\right)\kappa_{\mathrm{i}}\frac{I_m'(\kappa_{\mathrm{i}}a)}{I_m(\kappa_{\mathrm{i}}a)} - \left[(\omega - \mathbf{k}\cdot\mathbf{U})^2 - k_z^2 v_{\mathrm{Ai}}^2\right]\kappa_{\mathrm{e}}\frac{K_m'(\kappa_{\mathrm{e}}a)}{K_m(\kappa_{\mathrm{e}}a)} = 0. \tag{34}$$

For the azimuthal mode number $m = 0$ the above equation describes the propagation of so called *sausage* waves, while with $m = 1$ it governs the propagation of the *kink* waves (Edwin & Roberts, 1983). As we have already seen, the wave frequency, ω, is Doppler-shifted inside the jet. The two quantities κ_{i} and κ_{e}, whose squared magnitudes are given by Eq. (31) are termed *wave attenuation coefficients*. They characterize how quickly the wave amplitude having its maximal value at the interface, $r = a$, decreases as we go away in both directions. Depending on the specific sound and Alfvén speeds in a given medium, as well as on the density contrast, $\eta = \rho_{\mathrm{e}}/\rho_{\mathrm{e}}$, and the ratio of the embedded magnetic fields, $b = B_{\mathrm{e}}/B_{\mathrm{e}}$, the attenuation coefficients can be real or imaginary quantities. In the case when both κ_{i} and κ_{e} are real, we have a *pure surface wave*. The case κ_{i} imaginary and κ_{e} real corresponds to *pseudosurface waves* (or *body waves* according to Edwin & Roberts terminology (Edwin & Roberts, 1983)). In that case the modified Bessel function inside the jet, I_0, becomes the spatially periodic Bessel function J_0. In the opposite situation the wave energy is carried away from the flux tube – then the wave is called *leaky wave* (Cally, 1986). The waves, which propagate in spicules and X-ray jets, are generally pseudosurface waves, that can however, at some flow speeds become pure surface modes.

For the kink waves one defines the *kink speed* (Edwin & Roberts, 1983)

$$c_{\mathrm{k}} = \left(\frac{\rho_{\mathrm{i}} v_{\mathrm{Ai}}^2 + \rho_{\mathrm{e}} v_{\mathrm{Ae}}^2}{\rho_{\mathrm{i}} + \rho_{\mathrm{e}}}\right)^{1/2} = \left(\frac{v_{\mathrm{Ai}}^2 + (\rho_{\mathrm{e}}/\rho_{\mathrm{i}}) v_{\mathrm{Ae}}^2}{1 + \rho_{\mathrm{e}}/\rho_{\mathrm{i}}}\right)^{1/2}, \tag{35}$$

which is independent of sound speeds and characterizes the propagation of transverse perturbations.

Our study of the dispersion characteristics of kink and sausage waves, as well as their stability status will be performed in two steps. First, at given sound and Alfvén speeds inside the jet and its environment and a fixed flow speed U, we solve the transcendental dispersion Eq. (34) assuming that the wave angular frequency, ω, and the wave number, k_z, are real quantities. In the next step, when studying their stability/instability status, we assume that the wave frequency and correspondingly the wave phase velocity, $v_{\mathrm{ph}} = \omega/k_z$, become complex. Then, as the imaginary part of the complex frequency/phase velocity at a given wave number, k_z, and a critical jet speed, U_{crt}, has some non-zero positive value, one says that the wave becomes unstable – its amplitude begins to grow with time. In this case, the linear theory is no longer applicable and one ought to investigate the further wave propagation by means of a nonlinear theory. Our linear approach can determine just the instability threshold only.

In the next two section we numerically derive the dispersion curves of kink and sausage waves running along spicules and X-ray jets, respectively.

4. Dispersion diagrams of MHD surface waves in spicules

Before starting solving the wave dispersion relation (34), we have to specify some input parameters, characterizing both media (the jet and its surrounding). Bearing in mind, as we have already mention in the beginning of Sec. 2, the mass density of the environment is much less (50–100 times); thus we take the density contrast – the ratio of equilibrium plasma density outside to that inside of spicule – to be $\eta = 0.02$. Our choice of the sound and Alfvén speeds in the jet is $c_{\rm si} = 10\ {\rm km\,s^{-1}}$ and $v_{\rm Ai} = 80\ {\rm km\,s^{-1}}$, respectively, while those speeds in the environment are correspondingly $c_{\rm se} \cong 488\ {\rm km\,s^{-1}}$ and $v_{\rm Ae} = 200\ {\rm km\,s^{-1}}$. All these values are in agreement with the condition for the balance of total pressures at the flux tube interface – that condition can be expressed in the form

$$p_{\rm i} + \frac{B_{\rm i}^2}{2\mu} = p_{\rm e} + \frac{B_{\rm e}^2}{2\mu},$$

which yields (Edwin & Roberts (1983)

$$\frac{\rho_{\rm e}}{\rho_{\rm i}} = \frac{c_{\rm si}^2 + \frac{\gamma}{2} v_{\rm Ai}^2}{c_{\rm se}^2 + \frac{\gamma}{2} v_{\rm Ae}^2}. \tag{36}$$

The two tube speeds (look at Eq. (32)) are $c_{\rm Ti} = 9.9\ {\rm km\,s^{-1}}$ and $c_{\rm Te} = 185\ {\rm km\,s^{-1}}$. The kink speed, associated with the kink waves, in our case (see Eq. (35)) is $84\ {\rm km\,s^{-1}}$.

It is obvious that dispersion Eq. (34) of either mode can be solved only numerically. Before starting that job, we normalize all velocities to the Alfvén speed $v_{\rm Ai}$ inside the jet thus defining the dimensionless phase velocity $V_{\rm ph} = v_{\rm ph}/v_{\rm Ai}$ and the *Alfvén–Mach number* $M_{\rm A} = U/v_{\rm Ai}$. The wavelength is normalized to the tube radius a, which means that the dimensionless wave number is $K = k_z a$. The calculation of wave attenuation coefficients requires the introduction of three numbers, notably the two ratios $\bar{\beta} = c_{\rm s}^2/v_{\rm A}^2$ correspondingly in the jet and its environment, and the ratio of the background magnetic field outside to that inside the flow, $b = B_{\rm e}/B_{\rm i}$, in addition to the density contrast, η. We recall that the two $\bar{\beta}$s are 1.2 times smaller than the corresponding plasma betas in both media – the latter are given by the expressions

$$\beta_{\rm i,e} = 2\bar{\beta}_{\rm i,e}/\gamma.$$

Thus, the input parameters in the numerical procedure are

$$\eta = 0.02, \quad \bar{\beta}_{\rm i} \cong 0.016, \quad \bar{\beta}_{\rm e} \cong 5.96, \quad b \cong 0.35, \quad \text{and} \quad M_{\rm A}.$$

The value of the Alfvén–Mach number, $M_{\rm A}$, naturally depends on the value of the streaming velocity, U. Our choice of this value is $100\ {\rm km\,s^{-1}}$ that yields $M_{\rm A} = 1.25$. With these input values, we calculate the dispersion curves of first kink waves and then sausage ones.

4.1 Kink waves in spicules

We start by calculating the dispersion curves of kink waves assuming that the angular wave frequency, ω, is real. As a reference, we first assume that the plasma in the flux tube is static, i.e., $M_{\rm A} = 0$. The dispersion curves, which present the dependence of the normalized wave phase velocity on the normalized wave number, are in this case shown in Fig. 5. One can recognize three types of waves: a sub-Alfvénic slow magnetoacoustic wave (in

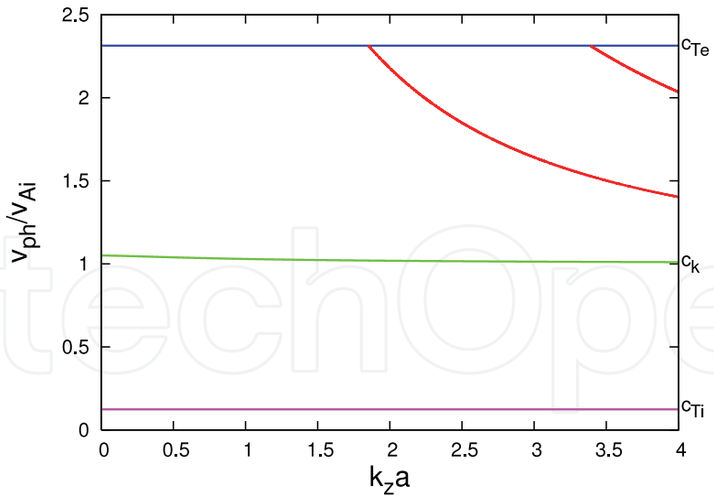

Fig. 5. Dispersion curves of kink waves propagating along the flux tube at $M_{\rm A} = 0$.

magenta colour) labelled c_{Ti} (which is actually the normalized value of $c_{\rm Ti}$ to $v_{\rm Ai}$), an almost Alfvén wave labelled c_k (the green curve), and a family of super-Alfvénic waves (the red dispersion curves). We note that one can get by numerically solving Eq. (34) the mirror images (with respect to the zeroth line) of the c_k-labelled dispersion curve, as well as of the fast super-Alfvénic waves – both being backward propagating modes that are not plotted in Fig. 5. The next Fig. 6 shows how all these dispersion curves change when the plasma inside the

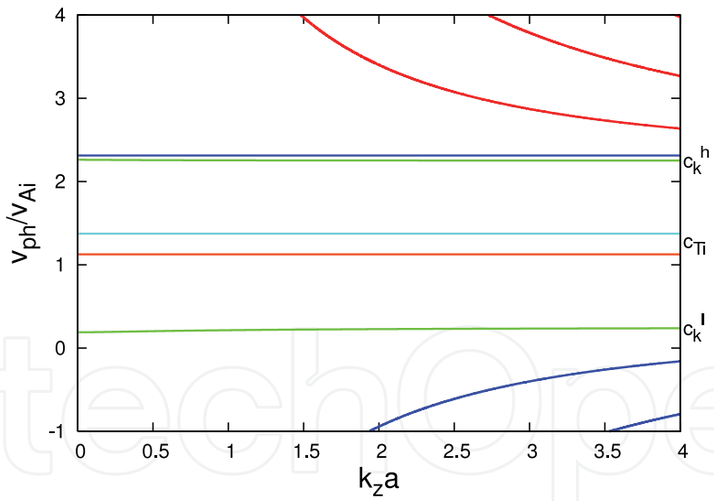

Fig. 6. Dispersion curves of kink waves propagating along the flux tube at $M_{\rm A} = 1.25$.

tube flows. One sees that the flow first shifts upwards the almost Alfvén wave now labelled $c_k^{\rm h}$, as well as high-harmonic super-Alfvénic waves. Second, the slow magnetoacoustic wave (c_{Ti} in Fig. 5) is replaced by two, now, super-Alfvénic waves, whose dispersion curves (in orange and cyan colours) are collectively labelled c_{Ti}. These two waves have practically constant normalized phase velocities equal to 1.126 and 1.374, respectively, which are the $(M_{\rm A} \mp c_{\rm Ti}^0)$-values, where $c_{\rm Ti}^0$ is the normalized magnitude of the slow magnetoacoustic wave at $M_{\rm A} = 0$. Unsurprisingly, one gets a $c_k^{\rm l}$-labelled curve, which is the mirror image of the $c_k^{\rm h}$-labelled curve. That is why this curve is plotted in green and, as can be seen, it is now

a forward propagating wave that has, however, a lower normalized phase velocity than that of its sister $\mathsf{c}_{\mathsf{k}}^{\mathsf{h}}$-labelled dispersion curve. Moreover, there appears to be a family of generally backward propagating waves (below the $\mathsf{c}_{\mathsf{k}}^{\mathsf{l}}$-labelled curve) plotted in blue colour that can similarly be considered as a mirror image of the high-harmonic super-Alfvénic waves.

The most interesting waves especially for the Type II spicules seems to be the waves labelled c_{k}. It would be interesting to see whether these modes can become unstable at some, say critical, value of the Alfvén–Mach number, M_{A}. To study this, we have to assume that the wave frequency is complex, i.e., $\omega \rightarrow \omega + \mathrm{i}\bar{\gamma}$, where $\bar{\gamma}$ is the expected instability growth rate. Thus, the dispersion equation becomes complex (complex wave phase velocity and real wave number) and the solving a transcendental complex equation is generally a difficult task (Acton, 1990).

Before starting to derive a numerical solution to the complex version of Eq. (34), we can simplify that equation. Bearing in mind that the plasma beta inside the jet is very small ($\beta_{\mathrm{i}} \cong 0.02$) and that of the surrounding medium quite high (of order 7), we can treat the jet as a cool plasma and the environment as a hot incompressible fluid. We point out that according to the numerical simulation of spicules by Matsumoto & Shibata (Matsumoto & Shibata, 2010) the plasma beta at heights greater than 2 Mm is of that order (0.03–0.04) – look at Fig. 4 in their paper. For cool plasma, $c_{\mathrm{s}} \rightarrow 0$; hence the normalized wave attenuation coefficient $\kappa_{\mathrm{i}} a = \left[1 - (V_{\mathrm{ph}} - M_{\mathrm{A}})^2\right]^{1/2} K$, while for the incompressible environment $c_{\mathrm{s}} \rightarrow \infty$ and the corresponding attenuation coefficient is simply equal to k_z, i.e., $\kappa_{\mathrm{e}} a = K$. Under these circumstances the simplified dispersion equation of kink waves takes the form

$$\left(V_{\mathrm{ph}}^2 \eta - b^2\right) \left[1 - \left(V_{\mathrm{ph}} - M_{\mathrm{A}}\right)^2\right]^{1/2} \frac{I_1'(\kappa_{\mathrm{i}} a)}{I_1(\kappa_{\mathrm{i}} a)} - \left[\left(V_{\mathrm{ph}} - M_{\mathrm{A}}\right)^2 - 1\right] \frac{K_1'(K)}{K_1(K)} = 0, \qquad (37)$$

where, we recall, that $\kappa_{\mathrm{i}} a = \left[1 - (V_{\mathrm{ph}} - M_{\mathrm{A}})^2\right]^{1/2} K$, and the normalized wave phase velocity, V_{ph}, is a complex number. We note that this simplified version of the dispersion equation of the kink waves closely reproduces the dispersion curves labelled c_{k} in Figs. 5 and 6.

To investigate the stability/instability status of kink waves we numerically solve Eq. (37) using the Müller method (Muller, 1956) for finding the complex roots at fixed input parameters $\eta = 0.02$ and $b = 0.35$ and varying the Alfvén–Mach number, M_{A}, from zero to some reasonable numbers. Before starting any numerical procedure for solving the aforementioned dispersion equation, we note that for each input value of M_{A} one can get two c_{k}-dispersion curves one of which (for relatively small magnitudes of M_{A}) has normalized phase velocity roughly equal to $M_{\mathrm{A}} - 1$ and a second dispersion curve associated with dimensionless phase velocity equal to $M_{\mathrm{A}} + 1$. These curves are similar to the dispersion curves labelled $\mathsf{c}_{\mathsf{k}}^{\mathsf{l}}$ and $\mathsf{c}_{\mathsf{k}}^{\mathsf{h}}$ in Fig. 6. The results of the numerical solving Eq. (37) are shown in Fig. 7. For $M_{\mathrm{A}} = 0$, except for the dispersion curve with normalized phase velocity approximately equal to 1, one can find a dispersion curve with normalized phase velocity close to -1 – that curve is not plotted in Fig. 7. Similarly, for $M_{\mathrm{A}} = 2$ one obtains a curve at $V_{\mathrm{ph}} = 1$ and another at $V_{\mathrm{ph}} = 3$, and so on. With increasing the magnitude of the Alfvén–Mach number kink waves change their structure – for small numbers being pseudosurface (body) waves and for $M_{\mathrm{A}} \geqslant 4$ becoming pure surface modes. Another effect associated with the increase in M_{A}, is that, for instance at $M_{\mathrm{A}} \geqslant 6$, the shapes of pairs of dispersion curves begin to visibly change as can be seen in Figs. 7 and 8. The most interesting observation is that for $M_{\mathrm{A}} \geqslant 8$ both curves begin to

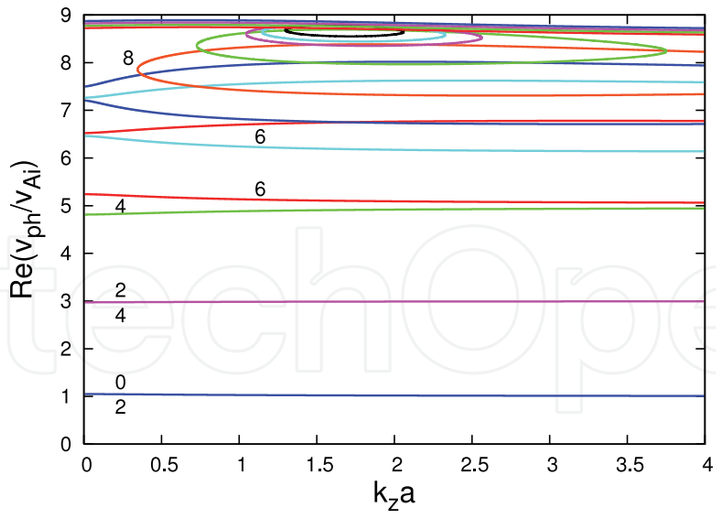

Fig. 7. Dispersion curves of kink waves propagating along the flux tube at various values of $M_{\rm A}$.

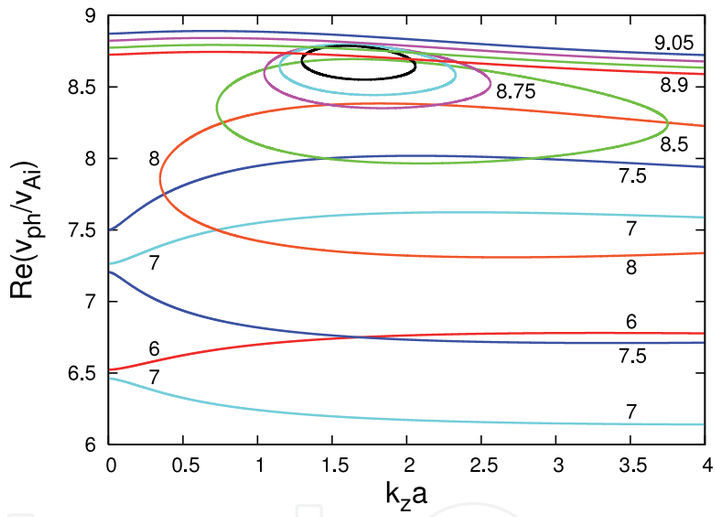

Fig. 8. Dispersion curves of kink waves propagating along the flux tube for relatively large values of $M_{\rm A}$.

merge and at $M_{\rm A} = 8.5$ they form a closed dispersion curve. The ever increasing of $M_{\rm A}$ yields yet smaller closed dispersion curves – the two non-labelled ones depicted in Fig. 8 correspond to $M_{\rm A} = 8.8$ and 8.85, respectively. All these dispersion curves present stable propagation of the kink waves. However, for $M_{\rm A} \geqslant 8.9$ we obtain a new family of wave dispersion curves that correspond to an unstable wave propagation. We plot in Fig. 8 four curves of that kind that have been calculated for $M_{\rm A} = 8.9$, 8.95, 9, and 9.05, respectively. The growth rates of the unstable waves are shown in Fig. 9. The instability that arises is of the Kelvin–Helmholtz type. We recall that the Kelvin–Helmholtz instability, which is named after Lord Kelvin and Hermann von Helmholtz, can occur when velocity shear is present within a continuous fluid, or when there is a sufficient velocity difference across the interface between two fluids (Chandrasekhar, 1961). In our case, we have the second option and the relative jet

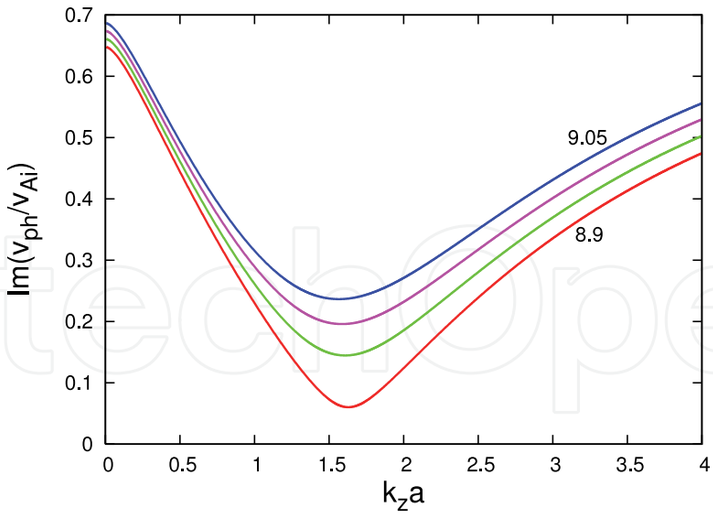

Fig. 9. Growth rates of unstable kink waves propagating along the flux tube at values of M_{A} equal to 8.9, 8.95, 9, and 9.05, respectively.

velocity, U, plays the role of the necessary velocity difference across the interface between the spicule and its environment.

The big question that immediately springs to mind is whether one can really observe such an instability in spicules. The answer to that question is obviously negative – to register the onset of a Kelvin–Helmholtz instability of kink waves travelling on a Type II spicule one would need to observe jet velocities of the order of or higher than 712 $\mathrm{km\,s^{-1}}$! If we assume that the density contrast, η, possesses the greater value of 0.01 (which means that the jet mass density is 100 times larger than that of the ambient medium) and the ratio of the background magnetic fields, b, is equal to 0.36 (which may be obtained from a slightly different set of characteristic sound and Alfvén speeds in both media), the critical Alfvén–Mach number at which the instability starts is even much higher (equal to 12.6) – in that case the corresponding jet speed is $U_{\mathrm{crt}} = 882\ \mathrm{km\,s^{-1}}$ – too high to be registered in a spicule. The value of 882 was computed under the assumption that the Alfvén speed inside the jet is 70 $\mathrm{km\,s^{-1}}$.

We note that very similar dispersion curves and growth rates of unstable kink waves like those shown in Figs. 8 and 9 were obtained for cylindrical jets when both media were treated as incompressible fluids. In that case, dispersion Eq. (37) becomes a quadratic equation

$$\left(V_{\mathrm{ph}}^2\eta - b^2\right)\frac{I_m'(K)}{I_m(K)} - \left[\left(V_{\mathrm{ph}} - M_{\mathrm{A}}\right)^2 - 1\right]\frac{K_m'(K)}{K_m(K)} = 0, \tag{38}$$

that provides solutions for the real and imaginary parts of the normalized wave phase velocity in closed forms, notably (Zhelyazkov, 2010; 2011)

$$V_{\mathrm{ph}} = \frac{-M_{\mathrm{A}}B \pm \sqrt{D}}{\eta A - B},$$

where

$$A = I_m'(K)/I_m(K), \qquad B = K_m'(K)/K_m(K),$$

and the discriminant D is

$$D = M_A^2 B^2 - (\eta A - B)\left[\left(1 - M_A^2\right) B - A b^2\right].$$

Obviously, if $D \geqslant 0$, then

$$\mathrm{Re}(V_{\mathrm{ph}}) = \frac{-M_A B \pm \sqrt{D}}{\eta A - B}, \qquad \mathrm{Im}(V_{\mathrm{ph}}) = 0,$$

else

$$\mathrm{Re}(V_{\mathrm{ph}}) = -\frac{M_A B}{\eta A - B}, \qquad \mathrm{Im}(V_{\mathrm{ph}}) = \frac{\sqrt{D}}{\eta A - B}.$$

We note that our choice of the sign of $\sqrt{D}$ in the expression of $\mathrm{Im}(V_{\mathrm{ph}})$ is plus although, in principal, it might also be minus – in that case, due to the arising instability, the wave's energy is transferred to the jet.

It is interesting to note that for our jet with $b = 0.35$ and $\eta = 0.02$ the quadratic dispersion Eq. (38) yields a critical Alfvén–Mach number for the onset of a Kelvin–Helmholtz instability equal to 8.87, which is lower than its magnitude obtained from Eq. (37). With this new critical Alfvén–Mach number, the required jet speed for the instability onset is $\cong$710 km s^{-1}. The most astonishing result, however, is the observation that the dispersion curves and the corresponding growth rates, when kink waves become unstable, – look at Figs. 10 and 11 – are very similar to those shown in Figs. 8 and 9. It is worth mentioning that for the

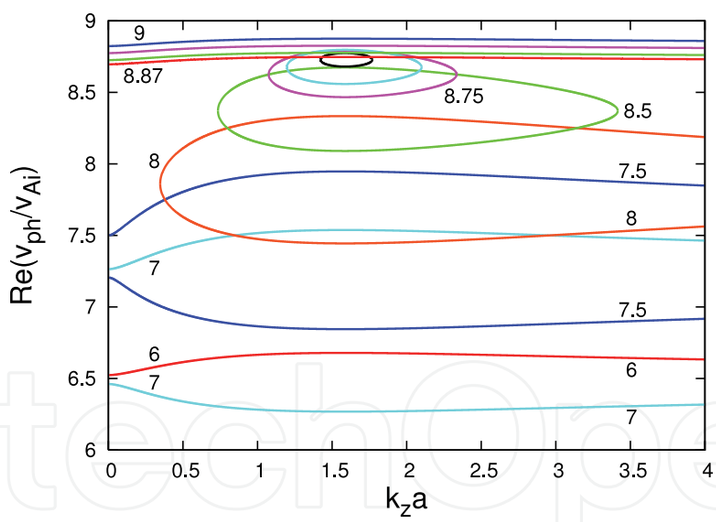

Fig. 10. Dispersion curves of kink waves derived from Eq. (38) for relatively large values of M_A.

same $\eta = 0.02$, but for $b = 1$ (equal background magnetic fields), the quadratic equation yields a much higher critical Alfvén–Mach number (=11.09), which means that the critical jet speed grows up to 887 km s^{-1}. This consideration shows that both the density contrast, η, and the ratio of the constant magnetic fields, b, are equally important in determining the critical Alfvén–Mach number. Moreover, since Eq. (37) and its simplified form as quadratic Eq. (38) yield almost similar results (both for dispersion curves and growth rates when kink waves become unstable) firmly corroborates the correctness of the numerical solutions to the complex dispersion Eq. (37).

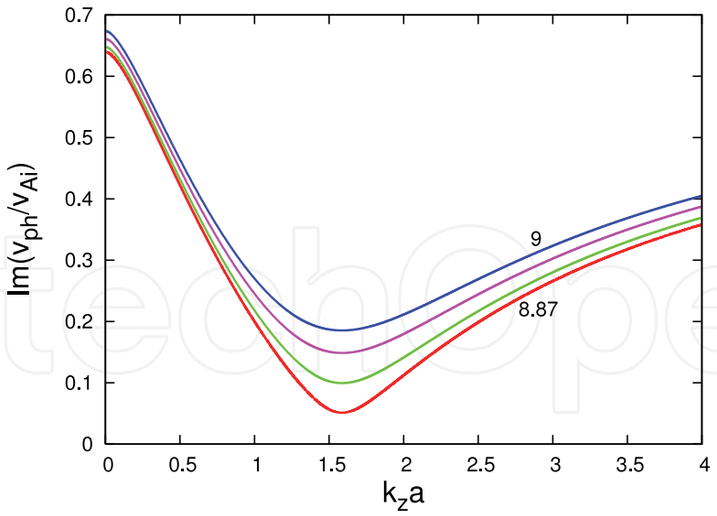

Fig. 11. Growth rates of unstable kink waves calculated from Eq. (38) at values of M_{A} equal to 8.87, 8.9, 8.95, and 9, respectively.

4.2 Sausage waves in spicules

The dispersion curves of sausage waves both in a static and in a flowing plasma shown in Figs. 12 and 13 are very similar to those of kink waves (compare with Figs. 5 and 6). The latter curves were calculated from dispersion Eq. (34) with azimuthal mode number $m = 0$ for the

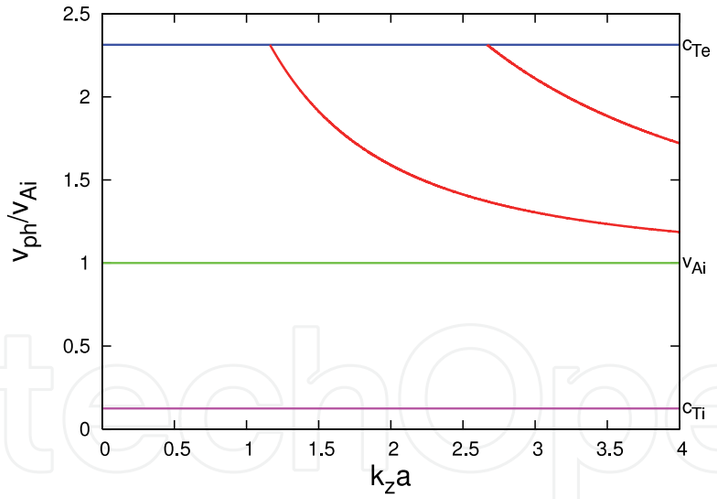

Fig. 12. Dispersion curves of sausage waves propagating along the flux tube at $M_{\mathrm{A}} = 0$.

same input parameters as in the case of kink waves. The main difference is that the c_k-labelled green dispersion curve is replaced by a curve corresponding to the Alfvén wave inside the jet. We note that the dispersion curve in Fig. 13 corresponding to a normalized phase velocity 0.25 is labelled $v_{\mathrm{Ai}}^{\mathrm{l}}$ because it can be considered as the one dispersion curve of the (1.25 ∓ 1)-curves that can be derived from the dispersion equation. As in the case of kink waves, the dispersion curve corresponding to the higher speed has the label $v_{\mathrm{Ai}}^{\mathrm{h}}$. Here we also get the two almost dispersionless curves collectively labelled c_{Ti} (in the same colours, orange and cyan, as in Fig. 6) with normalized wave phase velocities equal to 1.126 and 1.374.

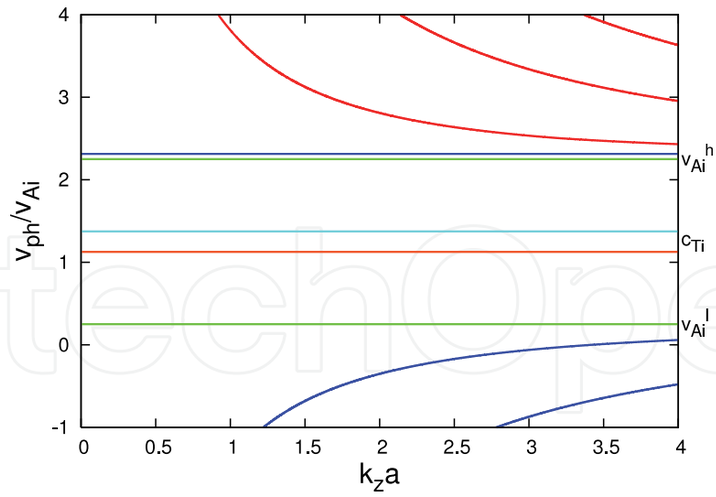

Fig. 13. Dispersion curves of sausage waves propagating along the flux tube at $M_{\rm A} = 1.25$.

When examining the stability properties of sausage waves as a function of the Alfvén–Mach number, $M_{\rm A}$, we use the same Eq. (37) while changing the order of the modified Bessel functions from 1 to 0. As in the case of kink waves, we are interested primarily in the behaviour of the waves whose phase velocities are multiples of the Alfvén speed. The results of numerical calculations of the complex dispersion equation are shown in Fig. 14. It turns out that for all reasonable Alfvénic Mach numbers the waves are stable. This is unsurprising

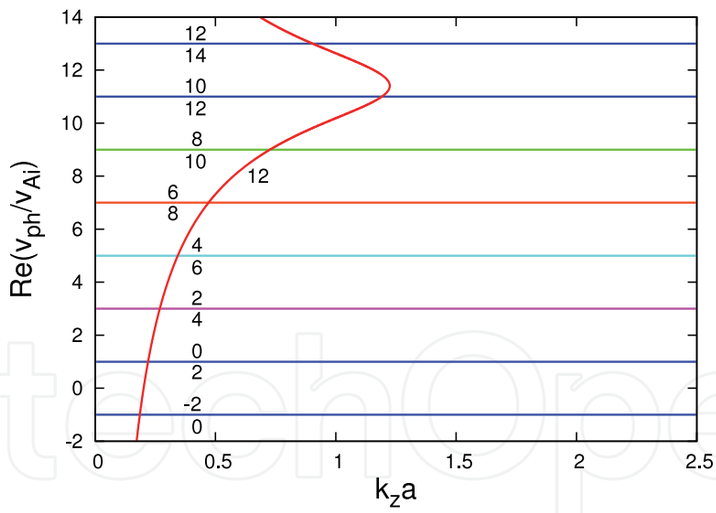

Fig. 14. Dispersion curves of sausage waves propagating along the flux tube at various values of $M_{\rm A}$.

because the same conclusion was drawn by solving precisely the complex dispersion equation governing the propagation of sausage waves in incompressible flowing cylindrical plasmas (Zhelyazkov, 2010; 2011). In Fig. 14 almost all dispersion curves have two labels: one for the $(\mathsf{M_A} - 1)$-labelled curve at given $M_{\rm A}$ (the label is below the curve), and second for the $(\mathsf{M}'_{\mathsf{A}} + 1)$-labelled curve associated with the corresponding $(M'_{\rm A} = M_{\rm A} - 2)$-value (the label is above the curve). This labelling is quite complex because for all $M_{\rm A}$ we find dispersion curves that overlap: for instance, the higher-speed dispersion curve (i.e., that associated with

the $(M_A + 1)$-value) for $M_A = 0$ coincides with the lower-speed dispersion curve (i.e., that associated with the $(M_A - 1)$-value) for $M_A = 2$. In contrast to the kink waves, which for $M_A \geqslant 4$ are pure surface modes, the sausage waves can be both pseudosurface and pure surface modes, or one of the pair can be a surface mode while the other is a pseudosurface one. For example, all dispersion curves for $M_A = 0$ and 8 correspond to the pseudosurface waves while the curves' pair associated with $M_A = 4$ describes the dispersion properties of pure surface waves. For the other Alfvén–Mach numbers, one of the wave is a pseudosurface and the other is a pure surface. However, there is a 'rule': if, for instance, the higher-speed wave with $M_A = 10$ is a pseudosurface mode, the lower-speed wave for $M_A = 12$ is a pure surface wave. We finish the discussion of sausage waves with the following conclusion: with increasing the Alfvén–Mach number M_A the initially independent high-harmonic waves and their mirroring counterparts begin to merge – this is clearly seen in Fig. 14 for $M_A = 12$ – the resulting dispersion curve is in red colour. A similar dispersion curve can be obtained, for example, for $M_A = 10$; the merging point of the corresponding two high-harmonic dispersion curves moves, however, to the right – it lies at $k_z a = 1.943$. It is also evident that in the long wavelength limit the bottom part of the red-coloured dispersion curve describes a backward propagating sausage pseudosurface wave. Another peculiarity of the same dispersion curve is the circumstance that for the range of dimensionless wave numbers between 0.7 and 1.23, one can have two different wave phase velocities. Which one is detected, the theory cannot predict.

5. Dispersion diagrams of MHD surface waves in soft X-ray jets

The geometry model of solar X-ray jets is the same as for the spicules – straight cylinder with radius a. Before starting the numerical calculations, we have to specify, as before, the input parameters. The sound and Alfvén speed that are typical for X-ray jets and their environment are correspondingly $c_{si} = 200\ \mathrm{km\,s^{-1}}$, $v_{Ai} = 800\ \mathrm{km\,s^{-1}}$, $c_{se} = 120\ \mathrm{km\,s^{-1}}$, and $v_{Ae} = 2300\ \mathrm{km\,s^{-1}}$. With these speeds the density contrast is $\eta = 0.13$. The same η (calculated from a slightly different set of sound and Alfvén speeds) Vasheghani Farahani et al. (Vasheghani Farahani et al., 2009) used in studying the propagation of transfer waves in soft X-ray coronal jets. Their analysis, however, is restricted to the long-wavelength limit, $|k|a \ll 1$ in their notation, while our approach considers the solving the exact dispersion relation without any limitations for the wavelength – such a treating is necessary bearing in mind that the wavelengths of the propagating along the jets fast magnetoacoustic waves might be of the order of X-ray jets radii. We remember that the soft X-ray coronal jets are much ticker than the Type II spicules.

With our choice of sound and Alfvén speeds, the tube velocities in both media (look at Eq. (32)), respectively, are $c_{Ti} \cong 194\ \mathrm{km\,s^{-1}}$ and $c_{Te} = 119.8\ \mathrm{km\,s^{-1}}$. The kink speed (see Eq. (35)) turns out to be rather high, namely $\cong 1078\ \mathrm{km\,s^{-1}}$. To compare our result of the critical jet speed for triggering the Kelvin–Helmholtz instability with that found by Vasheghani Farahani et al. (Vasheghani Farahani et al., 2009), we take the same jet speed as theirs, notably $U = 580\ \mathrm{km\,s^{-1}}$, which yields Alfvén–Mach number equal to 0.725. (For simplicity we assume that the ambient medium is static, i.e., $U_e = 0$.) Thus, our input parameters for the numerical computations are

$$\eta = 0.13, \quad \bar{\beta}_i \cong 0.06, \quad \bar{\beta}_e \cong 0.003, \quad b = 1.035, \quad \text{and} \quad M_A = 0.725.$$

We note that $b = 1.035$ means that the equilibrium magnetic fields inside and outside the X-ray coronal jet are almost identical. Moreover, due to the relatively small plasma betas, $\beta_e = 0.0033$ and $\beta_i = 0.075$, respectively, the magnetic pressure dominates the gas one in both media and the propagating waves along X-ray jets should accordingly be predominantly transverse.

5.1 Kink waves in soft X-ray coronal jets

The dispersion diagrams of kink waves propagating along a static-plasma ($U = 0$) flux tube are shown in Fig. 15. They, the dispersion curves, have been obtained by numerically finding

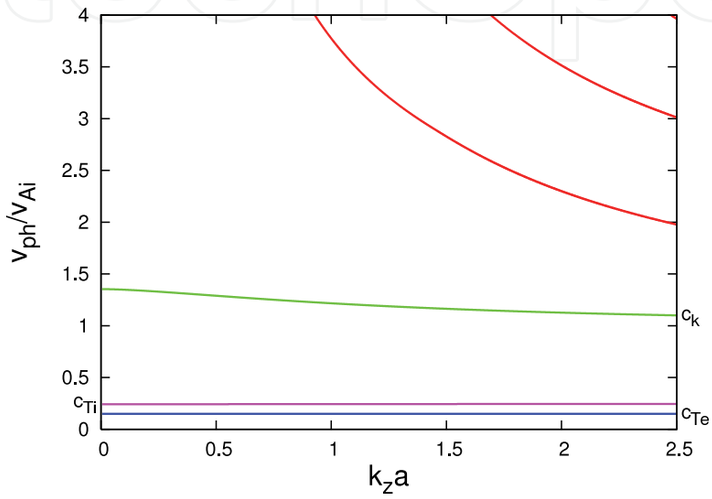

Fig. 15. Dispersion curves of kink waves propagating along a flux tube modelling X-ray jet at $M_A = 0$.

the solutions to dispersion Eq. (34) with mode number $m = 1$ and input data listed in the introductory part of this section with $M_A = 0$. The dispersion curves are very similar to those for spicules (look at Fig. 5). Here, there is, however, one distinctive difference: the c_{Te}-labelled dispersion curve (blue color) lies below the curve corresponding to the tube velocity inside the jet (magenta coloured line labelled c_{Ti}). The dispersion curves of the high-harmonic super-Alfvénic waves (red colour) lye, as usual, above the green curve associated with the kink speed. What actually does the flow change when is taken into account? The answer to this question is given in Fig. 16. As in the case with spicules, the flow duplicates the c_{Ti}-labelled dispersion curve in Fig. 15. The two, again collectively labelled c_{Ti} dispersion curves, are sub-Alfvénic waves having normalized phase velocities equal to 0.482 and 0.968 in correspondence to the $(M_A \mp c_{Ti}^0)$-rule. All the rest curves have the same behaviour and notation as in Fig. 6. The only difference here is the circumstance that the lower-speed c_k-curve lies below the zero line, i.e., it describes a *backward* propagating kink pseudosurface wave. This is because the Alfvén–Mach number now is less than one. We note also that the c_{Te}-labelled dispersion curve is unaffected by the presence of flow.

The most intriguing question is whether the c_k-labelled wave can become unstable at any reasonable flow velocity. Before answering that question, we have, as before, to simplify dispersion Eq. (34). Since the two plasma betas, as we have already mentioned, are much less that one, we can treat both media (the X-ray jet and its environment) as cool plasmas. In

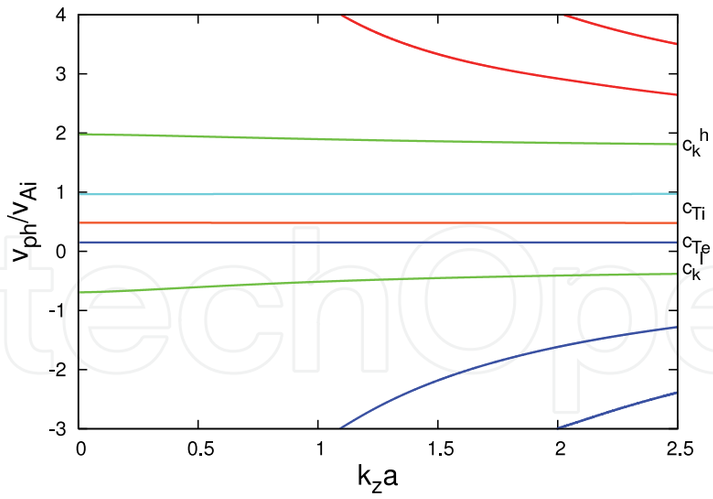

Fig. 16. Dispersion curves of kink waves propagating along a flux tube modelling X-ray jet at $M_{\rm A} = 0.725$.

this case, the simplified dispersion equation of kink waves (in complex variables!) takes the form

$$\left(V_{\rm ph}^2\eta - b^2\right)\left[1-\left(V_{\rm ph}-M_{\rm A}\right)^2\right]^{1/2}\frac{I_1'(\kappa_{\rm i}a)}{I_1(\kappa_{\rm i}a)}$$

$$-\left[\left(V_{\rm ph}-M_{\rm A}\right)^2-1\right]\left(1-V_{\rm ph}^2\eta\right)\frac{K_1'(\kappa_{\rm e}a)}{K_1(\kappa_{\rm e}a)}=0, \tag{39}$$

where

$$\kappa_{\rm i}a=\left[1-\left(V_{\rm ph}-M_{\rm A}\right)^2\right]^{1/2}K \qquad \text{and} \qquad \kappa_{\rm e}a=\left(1-V_{\rm ph}^2\eta\right)^{1/2}K.$$

We numerically solve this equation by varying the magnitude of the Alfvén–Mach number, $M_{\rm A}$, using as before the Müller method and the dispersion curves of both stable and unstable kink waves are shown in Fig. 17. In this figure, we display only the most interesting, upper, part of the dispersion diagram, where one can observe the changes in the shape of the dispersion curves related to the corresponding $c_{\rm k}$-speeds. First and foremost, the shape of the merging dispersion curves (labelled 4, 4.1, 4.2, and 4.23 in Fig. 17) is distinctly different from that of the similar curves in Fig. 8. Here, the curves, which are close to the dispersion curves corresponding to an unstable wave propagation (the first one is with label 4.25) are *semi-closed* in contrast to the closed curves in Fig. 8. The wave growth rates corresponding to Alfvén–Mach numbers 4.25, 4.3, 4.35, and 4.4 are shown in Fig. 18. As can be seen, the shape of those curves is completely different to that of the wave growth rates shown in Figs. 9 and 11. We note that all dispersion curves for $M_{\rm A} \geqslant 4$ correspond to pure surface kink waves.

It is clear from Figs. 17 and 18 that the critical Alfvén–Mach number, which determines the onset of a Kelvin–Helmholtz instability of the kink waves, is equal to 4.25 – the corresponding flow speed is 3400 km s^{-1}, that is much higher than the value we have used for calculating the dispersion curves in Fig. 16. The critical Alfvén–Mach number evaluated by Vasheghani Farahani et al. (Vasheghani Farahani et al., 2009), is 4.47, that means the corresponding flow speed must be at least 3576 km s^{-1}. If we use our Eq. (39) with the same $\rho_{\rm e}/\rho_{\rm i} = 0.13$, but

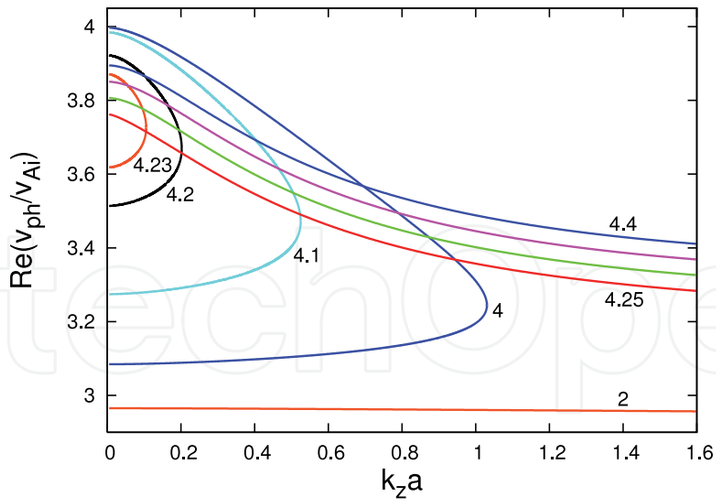

Fig. 17. Dispersion curves of kink waves propagating along a flux tube modelling X-ray jets for relatively large values of M_{A}.

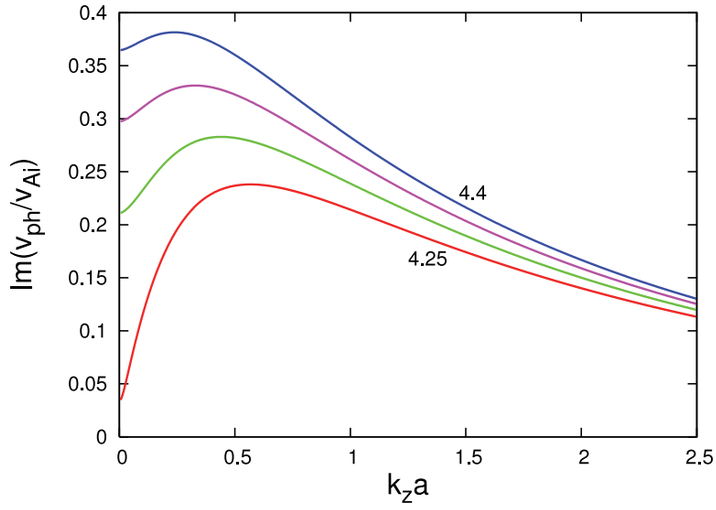

Fig. 18. Growth rates of unstable kink waves propagating along a flux tube modelling X-ray jets at values of M_{A} equal to 4.25, 4.3, 4.35, and 4.4, respectively.

with a little bit higher $B_{\mathrm{e}}/B_{\mathrm{i}} = 1.1132$, we get that the critical jet speed for triggering the Kelvin–Helmholtz instability in a soft X-ray coronal get would be $4.41 v_{\mathrm{Ai}} = 3528\ \mathrm{km\,s^{-1}}$. It is necessary, however, to point out that the correct density contrast that can be calculated from Eq. (36) with $c_{\mathrm{si}} = 360\ \mathrm{km\,s^{-1}}$, $v_{\mathrm{Ai}} = 800\ \mathrm{km\,s^{-1}}$, $c_{\mathrm{se}} = 120\ \mathrm{km\,s^{-1}}$, and $v_{\mathrm{Ae}} = 2400\ \mathrm{km\,s^{-1}}$ (the basic speeds in Vasheghani Farahani et al. paper) is $\rho_{\mathrm{e}}/\rho_{\mathrm{i}} = 0.137698$, which is closer to 0.14 rather than to 0.13. The solving Eq. (39) with the exact value of the density contrast (=0.1377) and the same $B_{\mathrm{e}}/B_{\mathrm{i}}$ as before (=1.1132) yields a critical flow speed equal to $4.31 v_{\mathrm{Ai}} = 3448\ \mathrm{km\,s^{-1}}$. All these calculations show that even small variations in the two ratios $\rho_{\mathrm{e}}/\rho_{\mathrm{i}}$ and $B_{\mathrm{e}}/B_{\mathrm{i}}$ lead to visibly different critical Alfvén–Mach numbers – our choice of the sound and Alfvén speeds gives the smallest value of the critical M_{A}. According to the more recent observations (Madjarska, 2011; Shimojo & Shibata, 2000), the soft X-ray coronal jets can have velocities above $10^3\ \mathrm{km\,s^{-1}}$ and it remains to be seen whether a speed of $3400\ \mathrm{km\,s^{-1}}$ can

trigger the onset of a Kelvin–Helmholtz instability of the kink surface waves running along the jets.

5.2 Sausage waves in soft X-ray coronal jets

The dispersion diagram of sausage waves in a static-plasma flux tube should be more or less similar to that of the kink waves under the same circumstances. Here, however, the green curve in Fig. 15, associated with the kink speed c_k, is now replaced by a dispersionless line

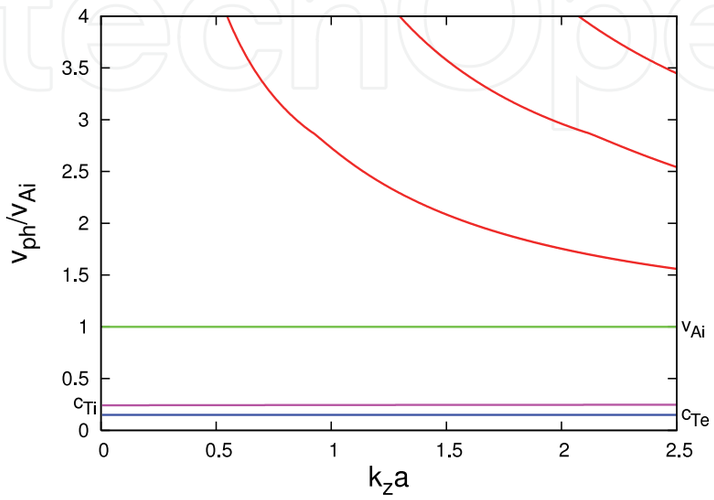

Fig. 19. Dispersion curves of sausage waves propagating along a flux tube modelling X-ray jet at $M_A = 0$.

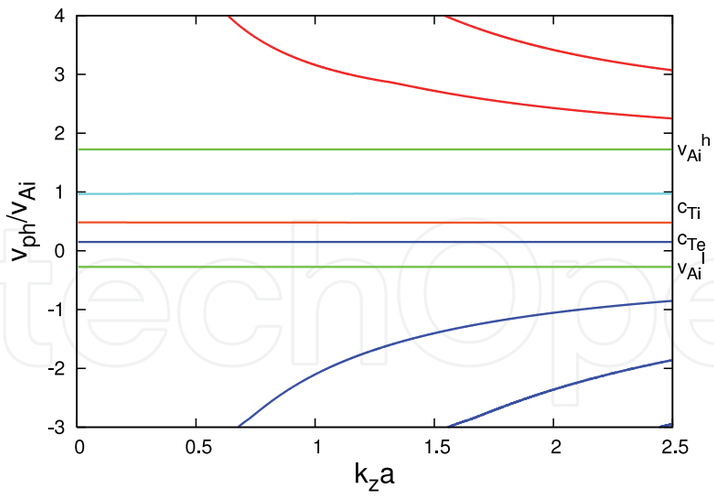

Fig. 20. Dispersion curves of sausage waves propagating along a flux tube modelling X-ray jet at $M_A = 0.725$.

related to the Alfvén speed – see the green curve in Fig. 19. Another difference is the number of the red-coloured high-harmonic super-Alfvénic waves – here it is 3 against 2 in Fig. 15. The dispersion diagram of the same mode in a flow with $M_A = 0.725$ ($U = 580$ km s^{-1}) is also predictable – the presence of the flow is the reason for splitting the green v_{Ai}-labelled curve

in Fig. 19 into two sister curves labelled, respectively, v^{l}_{Ai} and v^{h}_{Ai} – look at Fig. 20. Observe that the normalized speeds of those two waves are, as expected, equal to $M_A \mp 1$ – in our case the lower-speed Alfvén wave is a backward propagating one. The two sub-Alfvénic waves, whose dispersion curves are in orange and cyan colours and collectively labelled c_{Ti} have practically the same normalized phase velocities as the corresponding curves in Fig. 16. We note that one of the aforementioned curve is slightly decreasing (the orange curve) whilst the other, cyan-coloured, curve is slightly increasing when the normalized wave number $k_z a$ becomes larger – the same holds for the analogous waves in spicules. One can see in Fig. 20 a symmetry between the upper and bottom parts of the dispersion diagram – the 'mirror line' lies somewhere between the orange and cyan dispersion curves.

The 'evolution' of the green v_{Ai}-labelled curves in Fig. 20 with the increase in the Alfvén–Mach number is illustrated in Fig. 21. It is unsurprising that the sausage surface waves in soft X-ray

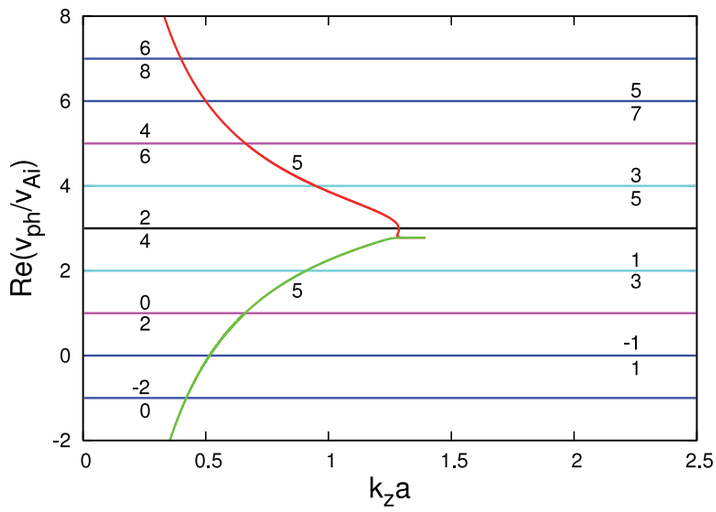

Fig. 21. Dispersion curves of sausage waves propagating along a flux tube modelling X-ray jets at various values of M_A.

coronal jets (like in spicules) are unaffected by the Kelvin–Helmholtz instability. Similarly as in Fig. 14, we have an overlapping of the dispersion curves associated with different Alfvén–Mach numbers. The labelling of dispersion curves in Fig. 21 is according to the previously discussed in Sec. 4.2 rule, namely each horizontal dispersion curve possesses two labels: one for the $(M_A - 1)$-curve at given M_A (the label is below the curve), and second for the $(M'_A + 1)$-curve associated with the corresponding $(M'_A = M_A - 2)$-value (the label is above the curve). Interestingly, even for the relatively low $M_A = 1$ both the lower- and the high-speed curves describe pure surface sausage waves. The same is also valid for the dispersion lines corresponding to Alfvén–Mach numbers equal to 4 and 5. The lower-speed Alfvénic curve at $M_A = 6$ is related to a pseudosurface sausage wave while the higher-speed one (with normalized phase velocity equal to 7) corresponds to a pure surface mode. (With $M_A = 2$ we have just the opposite situation.) At $M_A \geqslant 7$ all waves are pseudosurface ones. Each choice of the Alfvén–Mach number indeed requires separate studying of the wave's proper mode. Apart from Alfvénic waves and the pair of sub-Alfvénic modes (orange and cyan curves in Fig. 20), there appear to be families of high-speed harmonic waves (with red and blue colours of their dispersion curves), which also change with the increase of M_A. Initially being independent, with the growing of the Alfvén–Mach number, they change

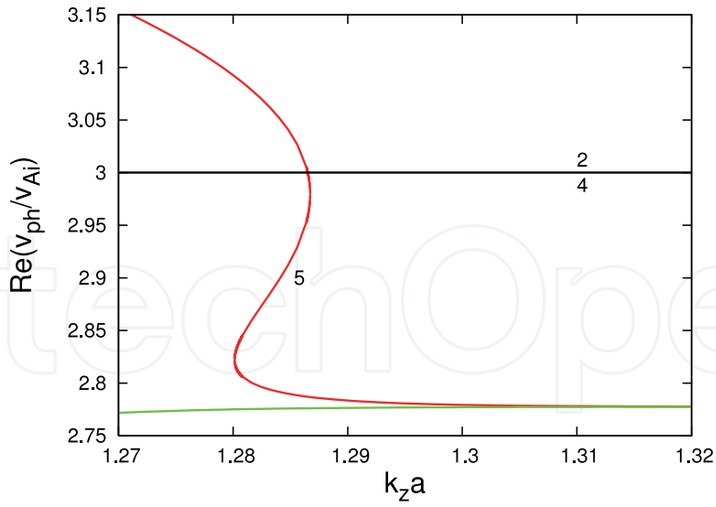

Fig. 22. Zoomed part of the dispersion diagram in Fig. 21 where two dispersion curves of super-Alfvénic sausage waves (at $M_{\rm A} = 5$) are touching each other.

their shapes and one may occur to observe the merging of, for instance, the first curves of each family as this has been shown in Fig. 14 (see the red curve there). Here, however, the situation is über-complicated – instead of merging we encounter a new phenomenon, notably the *touching* of two dispersion curves – see the green and red curves in Fig. 21 (calculated for $M_{\rm A} = 5$), and with more details in Fig. 22. The tip of the horizontal spike lies at $k_z a = 1.395$. Another peculiarity of this complex curve is the inverted-s shape of the red curve between the dimensionless wave numbers 1.28 and 1.29. Across that range, at a fixed $k_z a$, one can 'detect' four different normalized wave phase velocities. Similar sophisticated dispersion curves might also be obtained for $M_{\rm A} = 4$ or $M_{\rm A} = 6$. Maybe nowadays the sausage mode is not too interesting for the spacecrafts' observers but, who knows, it can sometime become important in interpretation observational data.

6. Conclusion

We now summarize the main findings of our chapter. We have studied the dispersion properties and the stability of the MHD normal modes running along the length of Type II spicules and soft X-ray coronal jets. Both have been modelled as straight cylindrical jets of ideal cool plasma surrounded by a warm/hot fully ionized medium (for spicules) or as flux tubes of almost cool plasma surrounded by a cool medium (for the X-ray jets). The wave propagation has been investigated in the context of standard magnetohydrodynamics by using linearized equations for the perturbations of the basic quantities: mass density, pressure, fluid velocity, and wave magnetic field. The derived dispersion equations describe the well-known kink and sausage mode influenced by the presence of spicules' or X-ray jets' moving plasma. The streaming plasma is characterized by its velocity **U**, which is directed along the background magnetic fields $\mathbf{B}_{\rm i}$ and $\mathbf{B}_{\rm e}$ inside the jet and in its environment. An alternative and more convenient way of specifying the jet is by defining the Alfvén–Mach number: the ratio of jet speed to the Alfvén speed inside the jet, $M_{\rm A} = U/v_{\rm Ai}$. The key parameters controlling the dispersion properties of the waves are the so-called density contrast, $\eta = \rho_{\rm e}/\rho_{\rm i}$, the ratio of the two background magnetic fields, $b = B_{\rm e}/B_{\rm i}$, and the two ratios of the squared sound and Alfvén speeds, $\bar{\beta}_{\rm e} = c_{\rm se}^2/v_{\rm Ae}^2$ and $\bar{\beta}_{\rm i} = c_{\rm si}^2/v_{\rm Ai}^2$. How does the

jet change the dispersion curves of both modes (kink and sausage waves) in a static-plasma flux tube? The answers to that question are as follows:

- The flow shifts upwards the specific dispersion curves, the kink-speed curve for kink waves and Alfvén-speed curve for sausage waves, as well as the high-harmonic fast waves of both modes. The sub-Alfvénic tube speed inside the jet, c_{Ti}, belongs to two waves with normalized phase velocities equal to $M_{\mathrm{A}} \mp c_{\mathrm{Ti}}/v_{\mathrm{Ai}}$. One also observes such a duplication of the c_{k}- or v_{Ai}-speed curve of kink or sausage waves. Below the lower-speed c_{k}- or v_{Ai}-curve there appears to be a set of dispersion curves, which are a mirror image of the high-harmonic fast waves. We note that the flow does not affect the c_{Te}-speed dispersion curve associated with the tube velocity in the environment.
- For a typical set of characteristic sound and Alfvén speeds in both media (the jet and its environment) at relatively small Alfvén–Mach numbers both modes are pseudosurface waves. With increasing M_{A}, some of them become pure surface waves. For kink waves, this finding is valid for $M_{\mathrm{A}} \geqslant 4$.
- The kink waves running along the jet can become unstable when the Alfvén–Mach number, M_{A}, exceeds some critical value. That critical value depends upon the two input parameters, η and b; the increase in the density contrast, $\rho_{\mathrm{e}}/\rho_{\mathrm{i}}$, decreases the magnitude of the critical Alfvén–Mach number, whilst the increase in the background magnetic fields ratio, $B_{\mathrm{e}}/B_{\mathrm{i}}$, leads to an increase in the critical M_{A}. For our choice of parameters for Type II spicules ($\eta = 0.02$ and $b = 0.35$) the value of the critical M_{A} is 8.9. This means that the speed of the jet must be at least 712 km s^{-1} for the onset of the Kelvin–Helmholtz instability of the propagating kink waves. Such high speeds of Type II spicules have not yet been detected. For the soft X-ray coronal jets, due to the greater density contrast ($\eta = 0.13$) and almost equal background magnetic fields ($b = 1.035$), the critical Alfvén–Mach number is approximately twice smaller (=4.25), but since the jet Alfvén speed is 10 times larger than that of spicules, the critical flow speed, U_{crt}, is much higher, namely 3400 km s^{-1}. Such high jet speeds can be in principal registered in soft X-ray coronal jets.

  A rough criterion for the appearance of the Kelvin–Helmholtz instability of kink waves is the satisfaction of an inequality suggested by Andries & Goossens (Andies & Goossens, 2001), which in our notation reads

$$M_{\mathrm{A}} > 1 + b/\sqrt{\eta}.$$

  This criterion provides more reliable predictions for the critical M_{A} when $b \approx 1$ (Zhelyazkov, 2010). In particular, for a X-ray jet with $\eta = 0.13$ and $b = 1.035$ the above criterion yields $M_{\mathrm{A}} > 3.87$, which is lower than the numerically found value of 4.25.
- The onset of the Kelvin–Helmholtz instability for kink surface waves running along a cylindrical jet, modelling a Type II spicule, is preceded by a substantial reorganization of wave dispersion curves. As we increase the Alfvén–Mach number, the pairs of high- and low-speed curves (look at Fig. 8) begin to merge transforming into closed dispersion curves. After a further increase in M_{A}, these closed dispersion curves become smaller – this is an indication that we have reached the critical M_{A} at which the kink waves are subjected to the Kelvin–Helmholtz instability – the unstable waves propagate across the entire $k_z a$-range having growth rates depending upon the value of the current M_{A}. We note that this behaviour has been observed for kink waves travelling on flowing solar-wind plasma (Zhelyazkov, 2010; 2011).

For the X-ray jets, the dispersion curves' reorganization, because the environment has been considered as a cool plasma, is different – now, at high enough flow speeds, the merging lower- and higher-speed c_k-dispersion curves take the form of semi-closed loops (see Fig. 17). As we increase the flow speed (or equivalently the Alfvén–Mach number), the semi-closed loops shrink and at some critical flow speed the kink wave becomes unstable and the instability is of the Kelvin–Helmholtz type. We note that the shapes of the waves' growth rates of kink waves in spicules and soft X-ray coronal jets are distinctly different – compare Figs. 9 and 18.

- We have found that the sausage waves are unaffected by the Kelvin–Helmholtz instability. This conclusion was also previously drawn for the sausage modes in flowing solar-wind plasma (Zhelyazkov, 2010; 2011).

As we have seen, very high jet speeds are required to ensure that the Kelvin–Helmholtz instability occurs for kink waves propagating in Type II spicules associated with a subsequent triggering of Alfvén-wave turbulence, hence the possibility that this mechanism is responsible for chromospheric/coronal heating has to be excluded. However, a twist in the magnetic field of the flux tube or its environment may have the effect of lowering the instability threshold (Bennett et al., 1999; Zaqarashvili et al., 2010) and eventually lead to the triggering of the Kelvin–Helmholtz instability. According to Antolin & Shibata (Antolin & Shibata, 2010), a promising way to ensure spicules'/coronal heating is by means of the mode conversion and parametric decay of Alfvén waves generated by magnetic reconnection or driven by the magneto-convection at the photosphere. However, spicules can be considered as Alfvén wave resonant cavities (Holweg, 1981; Leroy, 1981) and as Matsumoto & Shibata (Matsumoto & Shibata, 2010) claim, the waves of the period around 100–500 s can transport a large amount of wave energy to the corona. Zahariev & Mishonov (Zahariev & Mishonov, 2011) state that the corona may be heated through a self-induced opacity of high-frequency Alfvén waves propagating in the transition region between the chromosphere and the corona owing to a considerable spectral density of the Alfvén waves in the photosphere. Another trend in explaining the mechanism of coronal heating is the dissipation of Alfvén waves' energy by strong wave damping due to the collisions between ions and neutrals (Song & Vasyliūnas, 2011; Tsap et al., 2011). In particular, Song & Vasyliūnas, by analytically solving a self-consistent one-dimensional model of the plasma–neutral–electromagnetic system, show that the damping is extremely strong for weaker magnetic field and less strong for strong field. Under either condition, the high-frequency portion of the source power spectrum is strongly damped at the lower altitudes, depositing heat there, whereas the lower-frequency perturbations are nearly undamped and can be observed in the corona and above when the field is strong.

The idea that Alfvén waves propagating in the transition region can contribute to the coronal heating was firmly supported by the observational data recorded on April 25, 2010 by NASA's *Solar Dynamics Observatory* (see Fig. 2). As McIntosh et al. (McIntosh et al., 2011) claim, "*SDO* has amazing resolution, so you can actually see individual waves. Previous observations of Alfvénic waves in the corona revealed amplitudes far too small (0.5 $\mathrm{km\,s^{-1}}$) to supply the energy flux (100–200 $\mathrm{W\,m^{-2}}$) required to drive the fast solar wind or balance the radiative losses of the quiet corona. Here we report observations of the transition region (between the chromosphere and the corona) and of the corona that reveal how Alfvénic motions permeate the dynamic and finely structured outer solar atmosphere. The ubiquitous outward-propagating Alfvénic motions observed have amplitudes of the order of 20 $\mathrm{km\,s^{-1}}$

and periods of the order of 100–500 s throughout the quiescent atmosphere (compatible with recent investigations), and are energetic enough to accelerate the fast solar wind and heat the quiet corona."

Notwithstanding, as we have already mentioned in the end of Sec. 5.1, the possibility for the onset of a Kelvin–Helmholtz instability of kink waves running along soft X-ray coronal jets should not be excluded – at high enough flow speeds, which in principal are reachable, one can expect a dramatic change in the waves' behaviour associated with an emerging instability, and subsequently, with an Alfvén-wave-turbulence heating.

In all cases, the question of whether large coronal spicules can reach coronal temperatures remains open – for a discussion from an observational point of view we refer to the paper by Madjarska et al. (Madjarska et al., 2011).

7. References

Acton, F. S. (1990). *Numerical Methods That (Usually) Work*, Mathematical Association of America, ISBN: 0-88385-450-3, Washington, D.C., ch. 14.

Alfvén, H. (1942). Existence of Electromagnetic-Hydrodynamic Waves. *Nature*, Vol. 150, No. 3805, October 3 1942, 405–406.

Andries, J. & Goossens, M. (2001). Kelvin–Helmholtz instabilities and resonant flow instabilities for a coronal plume model with plasma pressure. *Astron. Astrophys.*, Vol. 368, No. 3, March IV 2001, 1083–1094.

Antolin, P. & Shibata, K. (2010). The Role of Torsional Alfvén Waves in Coronal Heating. *Astrophys. J.*, Vol. 712, No. 1, March 20 2010, 494–510.

Athay, R. G. & Holzer, T. E. (1982). Role of spicules in heating the solar atmosphere. *Astrophys. J.*, Vol. 255, April 15 1982, 743–752.

Athay, R. G. (2000). Are spicules related to coronal heating? *Solar Phys.*, Vol. 197, No. 1, November 2000, 31–42.

Beckers, J. M. (1968). Solar Spicules. *Solar Phys.*, Vol. 3, No. 3, March 1968, 367–433.

Beckers, J. M. (1972). Solar Spicules. *Ann. Rev. Astron. Astrophys.*, Vol. 10, September 1972, 73–100.

Bennett, K.; Roberts, B. & Narain, U. (1999). Waves in Twisted Magnetic Flux Tubes. *Solar Phys.*, Vol. 185, No. 1, March 1999, 41–59.

Cally, P. S. (1986). Leaky and non-leaky oscillations in magnetic flux tubes. *Solar Phys.*, Vol. 103, No. 2, February 1986, 277–298.

Centeno, R.; Bueno, J. T. & Ramos, A. A. (2010). On the Magnetic Field of Off-limb Spicules. *Astrophys. J.*, Vol. 708, No. 2, January 10 2010, 1579–1584.

Chandrasekhar, S. (1961). *Hydrodynamic and Hydromagnetic Stability*, Clarendon Press, ISBN: 0-486-64071-X, Oxford, ch. 11.

Chen, F. F. (1995). *Introduction to Plasma Physics*, Springer, ISBN: 0306307553, Berlin.

Cirtain, J. W.; Golub, L.; Lundquist, L. et al. (2007). Evidence for Alfvén Waves in Solar X-ray Jets. *Nature*, Vol. 318, No. 5856, December 7 2007, 1580–1582.

de Pontieu, B.; McIntosh, S.; Hansteen, V. H. et al. (2007). A Tale of Two Spicules: The Impact of Spicules on the Magnetic Chromosphere. *Publ. Astron. Soc. Japan*, Vol. 59, No. SP3, S655–S662.

De Pontieu, B.; McIntosh, S. W.; Carlsson, M. et al. (2011). The Origins of Hot Plasma in the Solar Corona. *Science*, Vol. 331, No. 6013, January 7 2011, 55–58.

Edwin, P. M. & Roberts, B. (1983). Wave Propagation in a Magnetic Cylinder. *Solar Phys.*, Vol. 88, Nos. 1–2, October 1983, 179–191.

Gekelman, W.; Vincena, S.; Van Compernolle, B.; Morales, G. J.; Maggs, J. E.; Pribyl, P. & Carter, T. A. (2011). The many faces of shear Alfvén waves. *Phys. Plasmas*, Vol. 18, No. 5, May 2011, 055501 (26 pages), doi: 10.1063/1.3592210.

He, J.-S.; Tu, C.-Y.; Marsch, E. et al. (1999). Upward propagating high-frequency Alfvén waves as identified from dynamic wave-like spicules observed by SOT on *Hinode*. *Astron. Astrophys.*, Vol. 497, No. 2, April II 2009, 525–535.

Hollweg, J. V. (1981). Alfvén waves in the solar atmosphere. *Solar Phys.*, Vol. 70, No. 1, March 1981, 25–66.

Kudoh, T. & Shibata, K. (1999). Alfvén Wave Model of Spicules and Coronal Heating. *Astrophys. J.*, Vol. 514, No. 1, March 20 1999, 493–505.

Kukhianidze, V.; Zaqarashvili, T. V. & Khutsishvili, E. (2006). Observation of kink waves in solar spicules. *Astron. Astrophys.*, Vol. 449, No. 2, April II 2006, L35–L38.

Leroy, B. (1981). Propagation of waves in an atmosphere in the presence of a magnetic field. III – Alfvén waves in the solar atmosphere. *Astron. Astrophys.*, Vol. 97, No. 2, April 1981, 245–250.

Madjarska, M. S. (2011). Dynamics and plasma properties of an X-ray jet from SUMER, EIS, XRT, and EUVI A & B simultaneous observations. *Astron. Astrophys.*, Vol. 526, February 2011, A19 (24 pages), doi: 10.1051/0004-6361/201015269.

Madjarska, M. S.; Vanninathan, K. & Doyle, J. D. (2011). Can coronal hole spicules reach coronal temperatures? *Astron. Astrophys.*, Vol. 532, August 2011, L1 (4 pages), doi: 10.1051/0004-6361/201116735.

Matsumoto, T. & Shibata, K. (2010). Nonlinear Propagation of Alfvén Waves Driven by Observed Photospheric Motion: Application to the Coronal Heating and Spicule Formation. *Astrophys. J.*, Vol. 710, No. 2, February 20 2010, 1857–1867.

McIntosh, S. W.; De Pontieu, B.; Carlsson, M.; Hansteen, V.; Boerner, P. & Goossens, M. (2011). Alfvénic waves with sufficient energy to power the quiet solar corona and fast solar wind. *Nature*, Vol. 475, No. 7357, July 28 2011, 477–480.

Moore, R. L.; Sterling, A. C.; Cirtain, J. W. & Falconer, D. A. (2011). Solar X-ray Jets, Type-II Spicules, Granule-size Emerging Bipoles, and the Genesis of the Heliosphere. *Astrophys. J.*, Vol. 731, No. 1, April 10 2011, L18 (5 pages), doi:10.1088/2041-8205/731/1/L18.

Muller, D. A. (1956). A Method for Solving Algebraic Equations Using an Automatic Computer. *Math. Tables Other Aids Comput.*, Vol. 10, No. 56, October 1956, 208–215.

Nakariakov, V. M. (2007). MHD oscillations in solar and stellar coronae: Current results and perspectives. *Adv. Space Res.*, Vol. 39, No. 12, December 2007, 1804–1813.

Roberts, W. O. (1945). A Preliminary Report on Chromospheric Spicules in Extremely Short Livetime. *Astrophys. J.*, Vol. 101, March 1945, 136R–140R.

Secchi, P. A. (1877). *Le Soleil*, 2nd edition, Part II, Gauthiers-Villars, Paris.

Shibata, K.; Ishido, Y.; Acton, L. W. et al. (1992). Observations of X-Ray Jets with the *Yohkoh* Soft X-Ray Telescope. *Publ. Astron. Soc. Japan*, Vol. 44, No. 5, October 1992, L173–L179.

Shimojo, M.; Hashimoto, S.; Shibata, K.; Hirayama, T.; Hudson, H. S. & Acton, L. W. (1996). Statistical Study of Solar X-Ray Jets Observed with the *Yohkoh* Soft X-Ray Telescope. *Publ. Astron. Soc. Japan*, Vol. 48, No. Sp1, February 1996, S123–S136.

Shimojo, M. & Shibata, K. (2000). Physical Parameters of Solar X-Ray Jets. *Astrophys. J.*, Vol. 542, No. 2, October 20 2000, 1100–1108.

Song, P. & Vasyliūnas, V. M. (2011). Heating of the solar atmosphere by strong damping of Alfvén waves. *J. Geophys. Res.*, Vol. 116, September 27 2011, A09104 (17 pages), doi: 10.1029/2011JA016679.

Sterling, A. C. (2000). Solar Spicules: A Review of Recent Models and Targets for Future Observations – (Invited Review). *Solar Phys.*, Vol. 196, No. 1, September 2000, 79–111.

Sterling, A. C.; Moore, R. L. & DeForest, C. E. (2010). *Hinode* Solar Optical Telescope observations of the source regions and evolution of "Type II" spicules at the solar limb. *Astrophys. J.*, Vol. 714, No. 1, May 1 2010, L1–L6.

Tavabi, E.; Koutchmy, S. & Ajabshirizadeh, A. (2011). A Statistical Analysis of the SOT-*Hinode* Observations of Solar Spicules and their Wave-like Behavior. *New Astron.*, Vol. 16, No. 4, July 2011, 296–305.

Terra-Homen, M.; Erdélyi, R. & Ballai, I. (2003). Linear and non-linear MHD wave propagation in steady-state magnetic cylinders. *Solar Phys.*, Vol. 217, No. 2, November 2003, 199–223.

Tsap, Y. T.; Stepanov, A. V. & Kopylova, Y. G. (2011). Energy Flux of Alfvén Waves in Weakly Ionized Plasma and Coronal Heating of the Sun. *Solar Phys.*, Vol. 270, No. 1, May 2011, 205–211.

van Ballegooijen, A. A.; Asgari-Targhi, M.; Cranmer, S. R. & DeLuca, A. A. (2011). Heating of the Solar Chromosphere and Corona by Alfvén Wave Turbulence. *Astrophys. J.*, Vol. 736, No. 1. July 20 2011, 3 (27 pages), doi: 10.1088/0004-637X/736/1/3.

Vasheghani Farahani, S.; Van Doorsselaere, T.; Verwichte, E. & Nakariakov, V. M. (2009). Propagating transverse waves in soft X-ray coronal jets. *Astron. Astrophys.*, Vol. 498, No. 2, May I 2009, L29–L32.

Zahariev, N. I. & Mishonov, T. M. (2011). Heating of the Solar Corona by Alfvén Waves: Self-Induced Opacity. *Proceedings of 3rd School and Workshop on Space Plasma Physics: AIP Conf. Proc.*, Vol. 1356, pp. 123–137, ISBN: 978-0-7354-0914-9, Kiten (Bulgaria), September 1–12, 2010, American Institute of Physics, Melville, NY 11747.

Zaqarashvili, T. V.; Khutsishvili, E.; Kukhianidze, V. & Ramishvili, G. (2007). Doppler-shift oscillations in solar spicules. *Astron. Astrophys.*, Vol. 474, No. 2, November I 2007, 627–632.

Zaqarashvili, T. V. & Erdélyi, R. (2009). Oscillations and Waves in Solar Spicules. *Space Sci. Rev.*, Vol. 149, Nos. 1–4, December 2009, 355–388.

Zaqarashvili, T. V.; Días, A. J.; Oliver, R. & Ballester, J. L. (2010). Instability of twisted magnetic tubes with axial mass flows. *Astron. Astrophys.*, Vol. 516, June–July 2010, A84 (8 pages), doi: 10.1051/0004-6361/200913874.

Zaqarashvili, T. V. (2011). Solar Spicules: Recent Challenges in Observations and Theory, *Proceedings of 3rd School and Workshop on Space Plasma Physics: AIP Conf. Proc.*, Vol. 1356, pp. 106–116, ISBN: 978-0-7354-0914-9, Kiten (Bulgaria), September 1–12, 2010, American Institute of Physics, Melville, NY 11747.

Zhelyazkov, I. (2010). Hall-magnetohydrodynamic waves in flowing ideal incompressible solar-wind plasmas. *Plasma Phys. Control. Fusion*, Vol. 52, No. 6, June 2010, 065008 (16 pages), doi: 10.1088/0741-3335/52/6/065008

Zhelyazkov, I. (2011). Hall-Magnetohydrodynamic Waves and their Stability in Flowing Solar-Wind Plasmas. *Proceedings of 3rd School and Workshop on Space Plasma Physics: AIP Conf. Proc.*, Vol. 1356, pp. 138–155, ISBN: 978-0-7354-0914-9, Kiten (Bulgaria), September 1–12, 2010, American Institute of Physics, Melville, NY 11747.

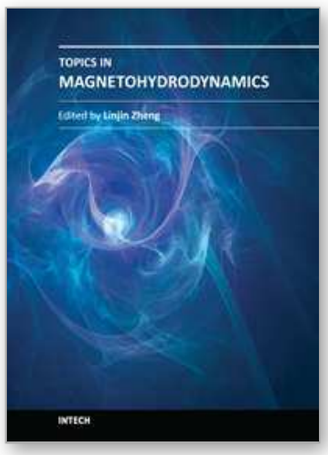

Topics in Magnetohydrodynamics

Edited by Dr. Linjin Zheng

ISBN 978-953-51-0211-3
Hard cover, 210 pages
Publisher InTech
Published online 09, March, 2012
Published in print edition March, 2012

To understand plasma physics intuitively one need to master the MHD behaviors. As sciences advance, gap between published textbooks and cutting-edge researches gradually develops. Connection from textbook knowledge to up-to-dated research results can often be tough. Review articles can help. This book contains eight topical review papers on MHD. For magnetically confined fusion one can find toroidal MHD theory for tokamaks, magnetic relaxation process in spheromaks, and the formation and stability of field-reversed configuration. In space plasma physics one can get solar spicules and X-ray jets physics, as well as general sub-fluid theory. For numerical methods one can find the implicit numerical methods for resistive MHD and the boundary control formalism. For low temperature plasma physics one can read theory for Newtonian and non-Newtonian fluids etc.

INTECH
open science | open minds

InTech Europe
University Campus STeP Ri
Slavka Krautzeka 83/A
51000 Rijeka, Croatia
Phone: +385 (51) 770 447
Fax: +385 (51) 686 166
www.intechopen.com

InTech China
Unit 405, Office Block, Hotel Equatorial Shanghai
No.65, Yan An Road (West), Shanghai, 200040, China
中国上海市延安西路65号上海国际贵都大饭店办公楼405单元
Phone: +86-21-62489820
Fax: +86-21-62489821

IntechOpen